Robust LQG/LTR-based Coordinated Control for a High-Fidelity Model of the Single-Machine Infinite-Bus System

Pratik Vernekar

***Abstract*—This paper presents a robust linear-quadratic-Gaussian/loop transfer recovery (LQG/LTR)-based coordinated controller for excitation and turbine-governor control in a single-machine infinite-bus (SMIB) system. The main goal of the controller is to enhance the transient stability and robustness of the SMIB system under large disturbances. The novelty of the proposed approach lies in its systematic progression from developing a physics-based, high-fidelity SMIB plant model that incorporates a synchronous generator, transient and sub-transient flux linkages, and turbine-governor dynamics for system validation to designing a reduced-order control-design model of the SMIB system for controller synthesis and stability analysis. The LQG/LTR approach utilizes Jacobian linearization, optimal control theory, and an enhanced Kalman filter, designed using the LTR procedure and a detailed frequency-domain loop-shaping analysis, alongside an iterative tuning and validation process across reduced-order and high-fidelity models, to achieve a reasonable balance between noise/disturbance rejection, robustness recovery, nominal system performance, and stability margins for the SMIB system. Rigorous simulations and comparative studies of the LQG/LTR and three nonlinear controllers are performed under different real-world operating scenarios, such as a three-phase short-circuit fault at the generator terminal and load variations. The simulation results for the high-fidelity SMIB plant model show that the proposed LQG/LTR strategy exhibits superior control performance compared to the three nonlinear controllers in terms of transient stability, convergence rate, rotor angle and frequency control, voltage regulation, and robustness under process and measurement noises, model uncertainties, severe faults, and load fluctuations.**

***Index Terms*—High-fidelity plant model, Kalman filter, LQG/LTR design, power system control, robust control, SMIB system.**

I. Introduction

THE modern power system, also known as the smart grid, is a highly complex, widely interconnected, large-scale nonlinear system. The stable and reliable operation of power systems has become increasingly challenging with the rapid integration of intermittent renewable energy sources like solar panels and wind turbines, distributed generation, energy storage systems, complex load profiles like plug-in electric vehicles, and advanced communication technologies into the smart grid. The overall stability of the power grid can be decomposed into the following objectives: 1) automatic voltage regulation (AVR) via excitation control; 2) rotor angle stability and load frequency control (LFC) via turbine-governor control; and 3) transient stability enhancement via coordinated control of the AVR and LFC loops in the event of severe faults, external disturbances, and system overload. Addressing the third objective through a coordinated control strategy that is robust to uncertainties is the most challenging due to the nonlinear and unmodeled dynamics, parametric variations, and load fluctuations of large interconnected power systems. In addition to multi-machine benchmark models like the IEEE 10-machine 39-bus New England test system [1], the single-machine infinite-bus (SMIB) system is often used to develop robust control strategies and conduct stability studies on the power grid because it captures the essential dynamics of the generator, turbine-governor system, and power network.

Many classical and advanced control strategies have been developed so far for the effective control and stability enhancement of SMIB and multi-machine power systems. Power system stabilizers have been widely used to enhance the power system's transient stability in response to minor disturbances by adding damping via excitation control modulation [2]. Novel control approaches using sliding mode control (SMC) [3]–[6] are used for the LFC design in power systems. The control methods in [2]–[6] are based on reduced-order power system models linearized around specific operating points. Therefore, these linear control methods cannot provide adequate damping and preserve transient stability over a wide range of operating conditions, particularly when power systems experience severe disturbances like three-phase short-circuit faults or sudden fluctuations in load demands. Also, the control approaches in [2]–[6] are not validated on high-fidelity plant models with uncertainties, which are closer reflections of practical multi-machine power systems. Furthermore, the control input chattering, saturation, and singularity problems in SMC-based LFC approaches [3]–[6] make them unfeasible for implementation on higher-order nonlinear power system models.

Nonlinear controllers, conversely, are unaffected by operating conditions and significantly enhance power system stability and transient performance across a broad spectrum of operating points, even amid severe disturbances or faults [7]–[25]. The feedback linearization technique, which can be broadly classified into three distinct forms, namely, direct feedback linearization control (DFLC), partial feedback linearization control (PFLC), and exact feedback linearization control (EFLC), has been widely used to design excitation controllers for SMIB and multi-machine power systems [7]–[22]. The DFLC methods utilized in [7]–[11] require measuring rotor angle, real and reactive power, real-time calculation

P. Vernekar is with General Motors, Milford, MI 48380, USA (e-mail: pratik.vernekar@gmail.com).

of higher-order derivatives, and designing virtual control inputs to cancel the system nonlinearities. This approach reduces the controller's robustness in the presence of measurement noise and external perturbations. Several PFLC techniques for SMIB and multi-machine power systems have been presented to address the limitations of the DFLC [12]–[18]. In [12]–[16], the synchronous generator's speed is used for the PFLC design, avoiding the challenges of rotor angle measurement and differentiator design in the DFLC [7]–[11] and PFLC procedures [17], [18]. The PFLC approach only partially linearizes higher-order dynamics in detailed generator models with many coupled differential equations. The remaining nonlinear dynamics, also known as the zero or internal dynamics, are not asymptotically stable in higher-fidelity power system models. Thus, employing the PFLC strategy to stabilize the zero dynamics of SMIB and multi-machine power systems with multiple interconnected generators is challenging due to the increased complexity and interdependencies. The EFLC method [19]–[22] minimizes the challenge of stabilizing the unstable internal dynamics of SMIB and interconnected multi-machine power systems, unlike PFLC-based approaches [12]–[18]. However, the EFLC technique involves the measurement of rotor angles of synchronous generators, which cannot be directly measured using sensors. Furthermore, the DFLC, PFLC, and EFLC schemes rely heavily on an accurate power system model and a precise knowledge of system nonlinearities. Consequently, these methods fail to achieve the desired stability or transient response in the presence of parametric variations in inertia, damping, transmission line reactance, and transient characteristics under different operating conditions. Additionally, they lack the robustness required to handle unmodeled plant dynamics, severe faults, and uncertainties effectively.

Adaptive and backstepping control techniques, including robust adaptive backstepping [23], extended backstepping [24], fractional-order SMC-based backstepping [25], and decentralized adaptive optimal output regulation [26], have been proposed to overcome the limitations of feedback linearization techniques (DFLC, PFLC, and EFLC) and to stabilize SMIB and multi-machine power systems. However, applying advanced adaptive and backstepping control techniques to power systems presents some challenges, such as parameter estimation and identification problems under disturbances and noise leading to incorrect adaptation and degraded control performance and excitation of unmodeled dynamics or high-frequency modes of the power system resulting in undesired oscillations.

Motivated by the above discussion, this paper presents a novel linear-quadratic-Gaussian/loop transfer recovery (LQG/LTR) strategy for coordinated control of the SMIB system's AVR and LFC loops to improve the transient response, stability, and robustness of the closed-loop system under severe faults, load fluctuations, and uncertainties. The proposed LQG/LTR technique achieves optimal control with good post-fault voltage regulation, enhances the system's robustness and stability under model uncertainties and disturbances, enables shaping of the loop transfer function for improved control over the system's frequency response, and estimates the unmeasurable states of the SMIB system using an enhanced Kalman filter. Ultimately, this study aims to develop a systematic framework for robust linear controller design for the SMIB system across diverse operating conditions that can be adapted to different power system configurations, providing greater control design flexibility.

Most controllers designed for SMIB and multi-machine power systems either utilize the classical third-order one-axis generator model for AVR via excitation control or simplified reduced-order power system models for LFC [2]–[13], [15], [16], [19]–[21], [24]–[27]. Higher-order power system models, including a two-axis fifth-order generator model in [14], [23], [28], a sixth-order generator-turbine model in [17], and a ninth-order SMIB system model with a seventh-order generator and second-order hydraulic turbine in [18], are used for controller design in some studies. We use first principles to develop a high-fidelity ninth-order model of the SMIB system, which comprises the synchronous generator, turbine, governor, transient and sub-transient flux linkages, and exciter system dynamics. This high-fidelity model serves as the plant or validation model and is not used for the controller design. We then present a fifth-order control-design model (CDM) of the SMIB system, which comprises the third-order one-axis generator model and a second-order turbine-governor model. The reduced-order CDM captures the key aspects and essential system dynamics of the high-fidelity plant model and is simple enough for robust controller design and stability studies of the SMIB system.

Next, to mitigate the drawbacks and enhance the robustness of the proposed linear [2]–[6], [26] and nonlinear [7]–[25] control strategies, we introduce a robust LQG/LTR control technique [29] that has been employed to reduce inter-area oscillations in multi-machine power systems [27], [28]. The LQG/LTR method utilizes an enhanced Kalman filter to estimate the rotor angle, the q-axis voltage, and the remaining unmeasurable states of the SMIB system. Since measuring the rotor angle of the synchronous generator in an interconnected multi-machine power system is challenging, we use the synchronous generator's speed, which can be directly measured using speed sensors, along with the terminal generator voltage, as outputs for the LQG/LTR controller design. Moreover, the speed, which is directly related to the derivative of the rotor angle, will provide more damping to the system when used as output feedback, similar to PFLC-based approaches [12]–[16]. The LQG/LTR technique employs covariance matrices reflecting fictitious process and measurement noise intensities as design parameters of the Kalman filter to account for uncertainties, unmodeled dynamics, and external disturbances. The Kalman filter gains are appropriately tuned using the LTR procedure to recover the robustness features of the full-state feedback linear quadratic regulator (LQR) at the plant input while achieving a reasonable trade-off between noise/disturbance rejection, closed-loop stability margin, and nominal system performance. The LQG controller gains are designed using optimal control theory to minimize the LQG cost function and maintain the SMIB system's closed-loop stability. A rigorous frequency domain loop-shaping analysis is used to fine-tune the gains of the proposed LQG/LTR

controller, which employs the loop transfer functions of the SMIB system's fifth-order linear CDM.

Finally, the LQG/LTR controller is validated on the reduced-order CDM and high-fidelity SMIB system plant models under different operating conditions, including a three-phase short-circuit fault at the generator terminal and variations in system load. We perform a comprehensive comparative analysis of the proposed LQG/LTR controller and three nonlinear controllers: the EFLC [19]–[22], the integral-EFLC (IEFLC) [22], and the PFLC [12]–[18], in terms of AVR, LFC, rotor angle stability, transient response, steady-state error, and robustness under various practical operating scenarios. We have chosen the EFLC, IEFLC, and PFLC approaches for the comparative study because they are the most widely used baseline nonlinear controllers for SMIB and multi-machine power systems. The extensive simulations and comparative studies demonstrate that the proposed LQG/LTR controller outperforms the EFLC, IEFLC, and PFLC approaches when validated on the high-fidelity SMIB plant model under different operating conditions. To the authors' best knowledge, the control synthesis methodology and comparative analysis of the proposed LQG/LTR controller in this paper are yet to be presented for the robust and optimal control of SMIB and multi-machine power systems.

The main contributions of this paper are as follows:

1) We provide a framework for developing a practical, empirical, and robust LQG/LTR controller for the SMIB system using a high-fidelity ninth-order physics-based plant model for validation and a fifth-order CDM of the SMIB system for controller synthesis. This controller is independent of the nonlinearities and unmodeled plant dynamics and can be adapted to develop control algorithms for multi-machine power systems and complex smart grids.

2) A detailed frequency domain loop-shaping design analysis of the LQG/LTR procedure, along with an iterative tuning and validation process across reduced-order and high-fidelity models, is performed to fine-tune the controller gains and obtain a reasonable balance between noise/disturbance rejection, robustness recovery, and stability margins for the SMIB system.

3) Extensive simulations compare the proposed LQG/LTR controller with three nonlinear controllers (EFLC, IEFLC, and PFLC) in terms of AVR, LFC, transient response, convergence rate, steady-state error, and robustness under different real-world operating scenarios such as severe power system faults and load variations.

II. High-Fidelity Model of the SMIB System

In an interconnected power system, where a synchronous generator powered by a turbine-governor system is connected to a power grid, there are two control loops: the automatic voltage regulator (AVR) loop and the load frequency control (LFC) loop. The controllers are set for a particular operating condition and accommodate changes in the load demand to maintain the frequency and voltage magnitude within the specified limits. Small changes in real power depend on changes in the rotor angle δ and thus the frequency ω. The reactive power depends on the voltage magnitude, i.e., the generator excitation. The synchronous generator consists of the following components: a) a stator with three-phase armature windings that supply power to the grid, b) a hydraulic turbine-driven rotor with an excitation field winding wrapped around it, and c) two short-circuit damper windings to dampen the rotor's mechanical oscillations.

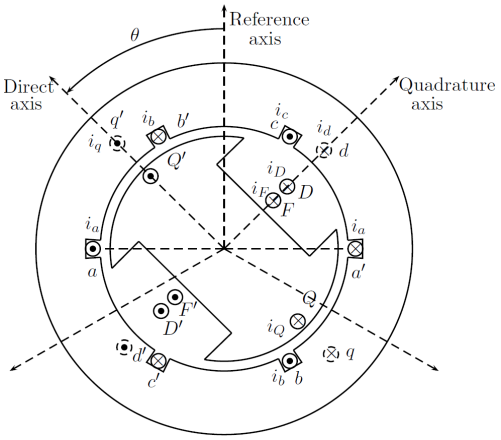

Fig. 1. Schematic of a synchronous generator [30].

A schematic of a synchronous generator with the reference directions is shown in Fig. 1 [30]. The armature winding, which carries the load current I_t and supplies power to the grid, is placed in equidistant slots on the inner surface of the stator and consists of three identical phase windings, namely, aa', bb', and cc'. The direct current (DC) excitation winding represented by FF' is wrapped around the rotor. The two short-circuit damper windings represented by DD' and QQ' help to dampen the rotor's mechanical oscillations. We define $\mathbf{v} = [v_a, v_b, v_c, -v_F, -v_D, -v_Q]^{\mathrm{T}}$ as the voltage vector consisting of the three-phase terminal voltages (v_a, v_b, v_c), the field winding voltage (v_F), and the voltages of the two damper windings (v_D, v_Q). The corresponding current vector is defined as $\mathbf{i} = [i_a, i_b, i_c, i_F, i_D, i_Q]^{\mathrm{T}}$.

A synchronous generator connected to an infinite bus through a transmission line with resistance R_e and inductance L_e is illustrated in [2], [7], [9], [15], [18], [21]. An infinite bus is an approximation of a large-scale interconnected power system where the action of a single generator will not affect the operation of the power grid. Additionally, a single-machine infinite-bus (SMIB) system, which is frequently employed for stability studies of multi-machine power systems, qualitatively manifests the principal features of a large interconnected power grid composed of numerous synchronous machines.

The electrical dynamics of the synchronous generator are obtained by using Park's transformation to transform variables from the static abc frame to a synchronously rotating dq frame. The infinite bus constraints are as follows [31]:

$$\begin{bmatrix} v_d \\ v_q \end{bmatrix} = R_e \begin{bmatrix} i_d \\ i_q \end{bmatrix} + L_e \begin{bmatrix} \dot{i}_d \\ \dot{i}_q \end{bmatrix} - \omega L_e \begin{bmatrix} -i_q \\ i_d \end{bmatrix} + \sqrt{3} V_\infty \begin{bmatrix} -\sin(\delta - \alpha) \\ \cos(\delta - \alpha) \end{bmatrix}, \tag{1}$$

in which α is the load angle, V_∞ is the infinite bus voltage, and v_d and v_q are the voltages along the synchronously rotating direct d-axis and quadrature q-axis in the dq frame,

respectively. Similarly, i_d and i_q are the d- and q-axis currents in the dq frame. Using (1), the electrical dynamics of a synchronous generator connected to an infinite bus can be written as follows:

$$\begin{bmatrix} L_d+L_e & kM_F & kM_D & 0 & 0 \\ -kM_F & -L_F & -M_R & 0 & 0 \\ -kM_D & -M_R & -L_D & 0 & 0 \\ 0 & 0 & 0 & L_q+L_e & kM_Q \\ 0 & 0 & 0 & -kM_Q & -L_Q \end{bmatrix} \begin{bmatrix} \dot{i}_d \\ \dot{i}_F \\ \dot{i}_D \\ \dot{i}_q \\ \dot{i}_Q \end{bmatrix} = \begin{bmatrix} -r-R_e & 0 & 0 & -\omega(L_q+L_e) & -\omega kM_Q \\ 0 & r_F & 0 & 0 & 0 \\ 0 & 0 & r_D & 0 & 0 \\ \omega(L_d+L_e) & \omega kM_F & \omega kM_D & -r-R_e & 0 \\ 0 & 0 & 0 & 0 & r_Q \end{bmatrix} \begin{bmatrix} i_d \\ i_F \\ i_D \\ i_q \\ i_Q \end{bmatrix} - \begin{bmatrix} 0 \\ v_F \\ 0 \\ 0 \\ 0 \end{bmatrix} - \sqrt{3}V_\infty \begin{bmatrix} -\sin(\delta-\alpha) \\ 0 \\ 0 \\ \cos(\delta-\alpha) \\ 0 \end{bmatrix}, \tag{2}$$

in which v_F is the excitation field voltage, $k=\sqrt{3/2}$ is the flux linkage constant, M_F is the mutual inductance between the dd' and FF' windings, M_D is the mutual inductance between the dd' and DD' windings, M_Q is the mutual inductance between the qq' and QQ' windings, M_R is the mutual inductance between the FF' and DD' windings, and L_d, L_F, L_D, L_q, and L_Q are the self-inductances of the dd', FF', DD', qq', and QQ' windings, respectively. Moreover, r is the resistance of each of the three-phase stator windings (aa', bb', and cc'), and r_F, r_D, and r_Q are the resistances of the FF', DD', and QQ' windings, respectively. Note that all the equations used to derive the high-fidelity model are in the per-unit (p.u.) system.

Next, the swing equation gives the mechanical dynamics of the synchronous generator in the p.u. system as follows [31]:

$$\begin{aligned} \dot{\omega} &= -\frac{(L_d i_d i_q + kM_F i_F i_q + kM_D i_D i_q - L_q i_d i_q)}{3\tau_j} \\ &\quad + \frac{kM_Q i_d i_Q}{3\tau_j} - \frac{1}{\tau_j}D\omega + \frac{1}{\tau_j}T_m, \\ \dot{\delta} &= \omega - 1, \end{aligned} \tag{3}$$

in which D is the damping constant, T_m is the mechanical torque of the turbine, $\tau_j = 2H\omega_R$, where H is the inertia constant, and ω_R is the base/reference angular velocity.

The dynamics of the turbine-governor system are given next [7]. The dynamics of the turbine in the p.u. system are

$$\dot{T}_m = -\frac{1}{\tau_T}T_m + \frac{K_T}{\tau_T}G_V, \tag{4}$$

in which G_V is the gate opening of the turbine, τ_T is the time constant of the turbine, and K_T is the gain of the turbine. The dynamics of the governor in the p.u. system are

$$\dot{G}_V = -\frac{1}{\tau_G}G_V + \frac{K_G}{\tau_G}\left(u_T - \frac{\omega}{R_T}\right), \tag{5}$$

in which u_T is the turbine valve control, τ_G is the time constant of the speed governor, K_G is the gain of the speed governor, and R_T is the regulation constant.

By combining the electrical and mechanical dynamics of the synchronous generator given in (2) and (3) with the turbine-governor dynamics described in (4) and (5), we obtain the ninth-order high-fidelity model of the SMIB system in the nonlinear state-space form as follows:

$$\begin{aligned} \dot{I}_d &= F_{11}I_d + F_{12}I_F + F_{13}I_D + F_{14}I_q\omega + F_{15}I_Q\omega \\ &\quad + F_{16}\sin(\delta-\alpha) + G_{11}V_F, \\ \dot{I}_F &= F_{21}I_d + F_{22}I_F + F_{23}I_D + F_{24}I_q\omega + F_{25}I_Q\omega \\ &\quad + F_{26}\sin(\delta-\alpha) + G_{21}V_F, \\ \dot{I}_D &= F_{31}I_d + F_{32}I_F + F_{33}I_D + F_{34}I_q\omega + F_{35}I_Q\omega \\ &\quad + F_{36}\sin(\delta-\alpha) + G_{31}V_F, \\ \dot{I}_q &= F_{41}I_d\omega + F_{42}I_F\omega + F_{43}I_D\omega + F_{44}I_q + F_{45}I_Q \\ &\quad + F_{46}\cos(\delta-\alpha), \\ \dot{I}_Q &= F_{51}I_d\omega + F_{52}I_F\omega + F_{53}I_D\omega + F_{54}I_q + F_{55}I_Q \\ &\quad + F_{56}\cos(\delta-\alpha), \\ \dot{\omega} &= F_{61}I_dI_q + F_{62}I_FI_q + F_{63}I_DI_q + F_{64}I_dI_Q + F_{65}\omega \\ &\quad + F_{66}T_m, \\ \dot{\delta} &= \omega - 1, \\ \dot{T}_m &= F_{81}T_m + F_{82}G_V, \\ \dot{G}_V &= F_{91}\omega + F_{92}G_V + G_{92}u_T, \end{aligned} \tag{6}$$

in which $F_{11} = -L_{d1}(r+R_e)$, $F_{12} = kM_{F1}r_F$, $F_{13} = kM_{D1}r_D$, $F_{14} = -(L_q+L_e)L_{d1}$, $F_{15} = -kM_QL_{d1}$, $F_{16} = V_\infty L_{d1}$, $G_{11} = -kM_{F1}$, $F_{21} = kM_{F1}(r+R_e)$, $F_{22} = -L_{F1}r_F$, $F_{23} = -M_{R1}r_D$, $F_{24} = kM_{F1}(L_q+L_e)$, $F_{25} = k^2M_{F1}M_Q$, $F_{26} = -V_\infty kM_{F1}$, $G_{21} = L_{F1}$, $F_{31} = kM_{D1}(r+R_e)$, $F_{32} = -M_{R1}r_F$, $F_{33} = -L_{D1}r_D$, $F_{34} = kM_{D1}(L_q+L_e)$, $F_{35} = k^2M_{D1}M_Q$, $F_{36} = -V_\infty kM_{D1}$, $G_{31} = M_{R1}$, $F_{41} = L_{q1}(L_d+L_e)$, $F_{42} = kM_FL_{q1}$, $F_{43} = kM_DL_{q1}$, $F_{44} = -L_{q1}(r+R_e)$, $F_{45} = kM_{Q1}r_Q$, $F_{46} = -V_\infty L_{q1}$, $F_{51} = -kM_{Q1}(L_d+L_e)$, $F_{52} = -k^2M_{Q1}M_F$, $F_{53} = -k^2M_{Q1}M_D$, $F_{54} = kM_{Q1}(r+R_e)$, $F_{55} = -L_{Q1}r_Q$, $F_{56} = V_\infty kM_{Q1}$, $F_{61} = -\frac{1}{\tau_j}(L_d-L_q)$, $F_{62} = -\frac{1}{\tau_j}kM_F$, $F_{63} = -\frac{1}{\tau_j}kM_D$, $F_{64} = \frac{1}{\tau_j}kM_Q$, $F_{65} = -\frac{1}{\tau_j}D$, $F_{81} = -\frac{1}{\tau_T}$, $F_{82} = \frac{K_T}{\tau_T}$, $F_{91} = -\frac{K_G}{\tau_GR_T}$, $F_{92} = -\frac{1}{\tau_G}$, $G_{92} = \frac{K_G}{\tau_G}$, $L_{d1} = \frac{1}{\mu}(M_R^2 - L_DL_F)$, $L_{F1} = \frac{1}{\mu}(M_D^2k^2 - L_D(L_d+L_e))$, $L_{D1} = \frac{1}{\mu}(M_F^2k^2 - L_F(L_d+L_e))$, $M_{F1} = \frac{1}{\mu}(M_DM_R - L_DM_F)$, $M_{D1} = \frac{1}{\mu}(M_FM_R - L_FM_D)$, $M_{R1} = \frac{1}{\mu}((L_d+L_e)M_R - M_DM_Fk^2)$, $L_{q1} = \frac{L_Q}{\nu}$, $L_{Q1} = \frac{L_e+L_q}{\nu}$, $M_{Q1} = \frac{M_Q}{\nu}$, $\mu = (L_d+L_e)M_R^2 - L_DL_F(L_d+L_e) + k^2(L_DM_F^2 + L_FM_D^2 - 2M_DM_FM_R)$, and $\nu = -k^2M_Q^2 + L_Q(L_e+L_q)$. In (6), the state variables i_d, i_F, i_D, i_q, i_Q, and the control input v_F have been converted to the corresponding root mean square (RMS) quantities I_d, I_F, I_D, I_q, I_Q, and V_F, by substituting $\frac{i_d}{\sqrt{3}} = I_d$, $\frac{i_F}{\sqrt{3}} = I_F$, $\frac{i_D}{\sqrt{3}} = I_D$, $\frac{i_q}{\sqrt{3}} = I_q$, $\frac{i_Q}{\sqrt{3}} = I_Q$, and $\frac{v_F}{\sqrt{3}} = V_F$. Let $x = [I_d, I_F, I_D, I_q, I_Q, \omega, \delta, T_m, G_V]^{\mathrm{T}}$ be the vector of state variables, $u = [V_F, u_T]^{\mathrm{T}}$ the vector of control inputs, and $y = [V_t, \omega]^{\mathrm{T}}$ the vector of outputs; then (6) can be written in the usual state-space form as follows:

$$\dot{x} = F(x) + G(x)u, \quad y = H(x), \quad \text{in which}$$

$$F(x) = \begin{bmatrix} F_{11}x_1 + F_{12}x_2 + F_{13}x_3 + F_{14}x_4x_6 + F_{15}x_5x_6 + F_{16}\sin(x_7-\alpha) \\ F_{21}x_1 + F_{22}x_2 + F_{23}x_3 + F_{24}x_4x_6 + F_{25}x_5x_6 + F_{26}\sin(x_7-\alpha) \\ F_{31}x_1 + F_{32}x_2 + F_{33}x_3 + F_{34}x_4x_6 + F_{35}x_5x_6 + F_{36}\sin(x_7-\alpha) \\ F_{41}x_1x_6 + F_{42}x_2x_6 + F_{43}x_3x_6 + F_{44}x_4 + F_{45}x_5 + F_{46}\cos(x_7-\alpha) \\ F_{51}x_1x_6 + F_{52}x_2x_6 + F_{53}x_3x_6 + F_{54}x_4 + F_{55}x_5 + F_{56}\cos(x_7-\alpha) \\ F_{61}x_1x_4 + F_{62}x_2x_4 + F_{63}x_3x_4 + F_{64}x_1x_5 + F_{65}x_6 + F_{66}x_8 \\ x_6 - 1 \\ F_{81}x_8 + F_{82}x_9 \\ F_{91}x_6 + F_{92}x_9 \end{bmatrix} \tag{7}$$

$$G(x) = \begin{bmatrix} G_{11} & 0 \\ G_{21} & 0 \\ G_{31} & 0 \\ 0 & 0 \\ 0 & 0 \\ 0 & 0 \\ 0 & G_{92} \end{bmatrix}$$

In (7), $x \in \mathbb{R}^9$, $u \in \mathbb{R}^2$, and $y \in \mathbb{R}^2$. Also, $F(x) : D \to \mathbb{R}^9$, $G(x) : D \to \mathbb{R}^{9\times 2}$, and $H(x) : D \to \mathbb{R}^{9\times 2}$ are sufficiently smooth on a domain $D \subset \mathbb{R}^9$. Thus, the SMIB is a multiple-input and multiple-output (MIMO) system with two inputs: the excitation field voltage V_F and the turbine valve control u_T, i.e., $u = [u_1, u_2]^{\mathrm{T}} = [V_F, u_T]^{\mathrm{T}}$, and two regulated outputs: the generator terminal voltage V_t and the angular frequency ω, i.e., $y = [y_1, y_2]^{\mathrm{T}} = [V_t, \omega]^{\mathrm{T}}$. The generator terminal voltage V_t is computed as $V_t = \sqrt{V_d^2 + V_q^2}$, in which the RMS quantities V_d and V_q are

$$\begin{aligned} V_d &= y_{11}I_d + y_{12}I_F + y_{13}I_D + y_{14}I_q\omega + y_{15}I_Q\omega \\ &\quad + y_{16}\sin(\delta-\alpha) + i_{11}V_F, \\ V_q &= y_{21}I_d\omega + y_{22}I_F\omega + y_{23}I_D\omega + y_{24}I_q + y_{25}I_Q \\ &\quad + y_{26}\cos(\delta-\alpha), \end{aligned} \tag{8}$$

where $y_{11} = R_e + L_eF_{11}$, $y_{12} = L_eF_{12}$, $y_{13} = L_eF_{13}$, $y_{14} = L_eF_{14} + L_e$, $y_{15} = L_eF_{15}$, $y_{16} = L_eF_{16} - V_\infty$, $i_{11} = L_eG_{11}$, $y_{21} = L_eF_{41} - L_e$, $y_{22} = L_eF_{42}$, $y_{23} = L_eF_{43}$, $y_{24} = R_e + L_eF_{44}$, $y_{25} = L_eF_{45}$, and $y_{26} = L_eF_{46} + V_\infty$.

The AVR control loop consists of the excitation field voltage V_F as the control input to regulate the generator terminal voltage V_t. Furthermore, the turbine valve control u_t and the turbine gate opening G_V work together to control the mechanical power output P_m of the turbine-governor system by modulating the fluid flow or gas intake via the regulated opening of the turbine-governor system's valves and gates. Consequently, the LFC loop consists of the turbine-governor control system to modulate the mechanical power output P_m and, thus, the frequency ω of the shaft that drives the rotor of the synchronous generator.

III. Control-Design Model of the SMIB System

The high-fidelity model of the SMIB system considers the load constraints, the excitation system, the mechanical torque of the turbine-speed governor system, and various effects introduced by the different rotor circuits, i.e., both field and damper-winding effects in the system model. Thus, the complete mathematical description of a large-scale multi-machine power system, which consists of numerous synchronous generators connected to the grid, is exceedingly complex and challenging to model. Simplifications are used to derive a reduced-order control-design model (CDM) of the SMIB system [30], which is then used to build robust controllers and conduct power grid stability studies. We now present a fifth-order CDM of the SMIB system, which consists of the classical third-order one-axis E'_q model of the synchronous generator [30], [31] and a second-order turbine-governor model [7]. The classical one-axis model of the generator ignores the damper winding effects, the d- and q-axis sub-transient flux linkages, and the d-axis transient flux linkage effects. This reduced-order CDM captures the salient features and characteristics of the complex high-fidelity SMIB system model while neglecting the less significant effects. At the same time, the CDM is simple enough for robust controller design and stability analysis of multi-machine power systems. The system equations for the nonlinear CDM are as follows:

$$\begin{aligned} \dot{E}'_q &= f_{11}E'_q + f_{12}\cos(\delta-\alpha) + f_{13}\sin(\delta-\alpha) \\ &\quad + g_{11}E_{FD}, \\ \dot{\omega} &= f_{21}E'^2_q + f_{22}E'_q\cos(\delta-\alpha) + f_{23}E'_q\sin(\delta-\alpha) \\ &\quad + f_{24}\sin(\delta-\alpha)\cos(\delta-\alpha) + f_{25}\cos^2(\delta-\alpha) \\ &\quad + f_{26}\sin^2(\delta-\alpha) + f_{27}\omega + f_{28}T_m, \\ \dot{\delta} &= \omega - 1, \\ \dot{T}_m &= f_{41}T_m + f_{42}G_V, \\ \dot{G}_V &= f_{51}\omega + f_{52}G_V + g_{55}u_T, \end{aligned} \tag{9}$$

in which

$$f_{11} = \frac{-(1+\frac{L_2L_1}{M_1})}{\tau'_{d0}},\ f_{12} = \frac{L_2L_1V_\infty}{M_1\tau'_{d0}},\ f_{13} = \frac{L_2R_1V_\infty}{M_1\tau'_{d0}},$$

$$g_{11} = \frac{1}{\tau'_{d0}},\ L_1 = L_q + L_e,\ L_2 = L_d - L'_d,\ L_3 = L'_d + L_e,$$

$$L_4 = L_q - L'_d,\ M_1 = (r+R_e)^2 + (L'_d + L_e)(L_q + L_e),$$

$$R_1 = r + R_e,\ \tau'_{d0} = \frac{L_F}{r_F},\ f_{21} = -\left(\frac{R_1}{M_1\tau_j} + \frac{L_4L_1R_1}{M_1^2\tau_j}\right),$$

$$f_{22} = \left(\frac{R_1}{M_1\tau_j} + \frac{2L_4L_1R_1}{M_1^2\tau_j}\right)V_\infty,\ f_{51} = -\frac{K_G}{\tau_GR_T},$$

$$f_{23} = -\left(\frac{L_3}{M_1\tau_j} + \frac{L_4L_1L_3}{M_1^2\tau_j} - \frac{L_4R_1^2}{M_1^2\tau_j}\right)V_\infty,\ f_{52} = -\frac{1}{\tau_G},$$

$$f_{24} = -\left(\frac{L_4R_1^2}{M_1^2\tau_j} - \frac{L_4L_1L_3}{M_1^2\tau_j}\right)V_\infty^2,\ g_{55} = \frac{K_G}{\tau_G},$$

$$f_{25} = -\left(\frac{L_4L_1R_1V_\infty^2}{M_1^2\tau_j}\right),\ f_{26} = \left(\frac{L_4L_3R_1V_\infty^2}{M_1^2\tau_j}\right),$$

$$f_{27} = -\frac{D}{\tau_j},\ f_{28} = \frac{1}{\tau_j},\ f_{41} = -\frac{1}{\tau_T},\ f_{42} = \frac{K_T}{\tau_T}.$$

and E'_q is the q-axis voltage behind the transient reactance L'_d, where $L'_d = L_d - \frac{(kM_F)^2}{L_F}$. The q-axis voltage E'_q cannot be physically measured in a practical system. Let us define the state variables as $x = [E'_q, \omega, \delta, T_m, G_V]^{\mathrm{T}}$, and the two

control inputs as $u = [u_1, u_2]^{\mathrm{T}} = [E_{FD}, u_T]^{\mathrm{T}}$. Thus, (9) can be written in the usual state-space form as follows:

$$\dot{x} = f(x) + g(x)u, \quad y = h(x), \quad \text{in which}$$

$$f(x) = \begin{bmatrix} f_{11}x_1 + f_{12}\cos(x_3-\alpha) + f_{13}\sin(x_3-\alpha) \\ [f_{21}x_1^2 + f_{22}x_1\cos(x_3-\alpha) + f_{23}x_1\sin(x_3-\alpha) \\ +f_{24}\sin(x_3-\alpha)\cos(x_3-\alpha) + f_{25}\cos^2(x_3-\alpha) \\ +f_{26}\sin^2(x_3-\alpha) + f_{27}x_2 + f_{28}x_4] \\ x_2 - 1 \\ f_{41}x_4 + f_{42}x_5 \\ f_{51}x_2 + f_{52}x_5 \end{bmatrix} \tag{10}$$

$$g(x) = \begin{bmatrix} g_{11} & 0 \\ 0 & 0 \\ 0 & 0 \\ 0 & 0 \\ 0 & g_{55} \end{bmatrix}.$$

In (10), $x \in \mathbb{R}^5$, $u \in \mathbb{R}^2$, and $y \in \mathbb{R}^2$. Thus, the reduced-order CDM of the SMIB is a MIMO system with two inputs: the excitation field electromagnetic force (EMF) E_{FD} and the turbine valve control u_T, and two outputs: the generator terminal voltage V_t and the angular frequency ω. The generator terminal voltage V_t is computed as $V_t = \sqrt{V_d^2 + V_q^2}$, in which V_d and V_q are computed as follows:

$$V_d = V_{d1}E'_q + V_{d2}\cos(\delta-\alpha) + V_{d3}\sin(\delta-\alpha),$$
$$V_q = V_{q1}E'_q + V_{q2}\cos(\delta-\alpha) + V_{q3}\sin(\delta-\alpha) + E'_q,$$

in which

$$\begin{aligned} V_{d1} &= -\frac{L_q(r+R_e)}{(r+R_e)^2 + (L'_d+L_e)(L_q+L_e)}, \\ V_{d2} &= \frac{V_\infty L_q(r+R_e)}{(r+R_e)^2 + (L'_d+L_e)(L_q+L_e)}, \\ V_{d3} &= -\frac{V_\infty L_q(L'_d+L_e)}{(r+R_e)^2 + (L'_d+L_e)(L_q+L_e)}, \\ V_{q1} &= -\frac{L'_d(L_q+L_e)}{(r+R_e)^2 + (L'_d+L_e)(L_q+L_e)}, \\ V_{q2} &= \frac{V_\infty L'_d(L_q+L_e)}{(r+R_e)^2 + (L'_d+L_e)(L_q+L_e)}, \\ V_{q3} &= \frac{V_\infty L'_d(r+R_e)}{(r+R_e)^2 + (L'_d+L_e)(L_q+L_e)}. \end{aligned} \tag{11}$$

IV. Robust LQG/LTR Control

The DFLC [7]–[11], EFLC [19]–[22], and PFLC [17], [18] methods require the measurement of rotor angles δ of synchronous generators, along with other measurable and quantifiable variables for controller design. However, rotor angles of synchronous generators cannot be directly measured, and sensor-based techniques often introduce noise and inaccuracies. Additionally, sensors are expensive and difficult to operate, making real-time rotor angle measurement impractical in multi-machine power systems. To overcome the above problem, we use the synchronous generator's speed or angular velocity ω, which can be directly measured using speed sensors, as the system output for the controller design [12]–[16]. Also, the angular velocity, which is directly related to the derivative of the rotor angle, will provide more damping to the system when used as output feedback. To accomplish this goal, we propose a robust LQG/LTR control technique that uses an enhanced Kalman filter to estimate the rotor angle and the remaining unmeasurable states of the SMIB system. The LQG/LTR is a robust linear control approach developed by Doyle [29] that uses an appropriately designed Kalman filter to recover the robustness features of the full-state feedback LQR at the plant input. We now present the LQG/LTR design strategy for the SMIB system.

- **Framework for robust LQG/LTR controller design**

The flowchart in Fig. 2 illustrates a step-by-step iterative process for developing and validating a robust LQG/LTR controller for a detailed model of the SMIB system, while Fig. 3 displays its block diagram. The novelty of the proposed LQG/LTR strategy lies in its systematic approach to designing and validating a robust controller for a complex power system, moving from a detailed model to a simplified one and then back to the detailed model for final validation. The SMIB system (plant) includes the governor, turbine, synchronous generator, and power grid or infinite bus. The LTR/LQG controller uses a Kalman filter to estimate unmeasurable states in conjunction with LQR control, resulting in optimal performance. Additionally, the LTR technique improves robustness by shaping the controller's frequency response, ensuring the controller maintains stability margins under process and measurement noises, uncertainties, model mismatches, and disturbances. The framework systematically progresses from developing a high-fidelity nonlinear model to designing a reduced-order CDM, allowing for practical controller synthesis while capturing essential system dynamics and ensuring the controller is robust and computationally efficient.

Furthermore, the gain scheduling strategy automatically adjusts controller gains based on varying operating conditions and can enhance the controller's effective range, thereby improving adaptability to real-world power system variations. This study does not consider enhancing the LQG/LTR method using the gain scheduling mechanism. The iterative tuning and validation process across reduced-order and high-fidelity models ensures optimal performance by balancing robustness, disturbance rejection, and system stability. As illustrated in the step-by-step flowchart in Fig. 2 and the detailed block diagram in Fig. 3, this integrated approach provides a comprehensive framework for designing high-performance, resilient controllers for SMIB and multi-machine power systems.

- **Step 1: Linearization of the SMIB system model**

The SMIB system's reduced-order CDM (10) is linearized around a nominal operating point (x_0, u_0) via the Jacobian linearization approach. The operating condition, which is a steady-state equilibrium of the system, is attained by the system after all the transients die out or decay to zero. The equilibrium point (x_0, u_0) is computed by solving the differential equation $\dot{x} = f(x_0) + g(x_0)u_0 = 0$. The reduced-order linearized model of the SMIB system can be written as follows:

$$\begin{aligned} \dot{x} &= Ax + Bu + d_1 + v_1, \\ y &= Cx + Du + d_2 + v_2, \end{aligned} \tag{12}$$

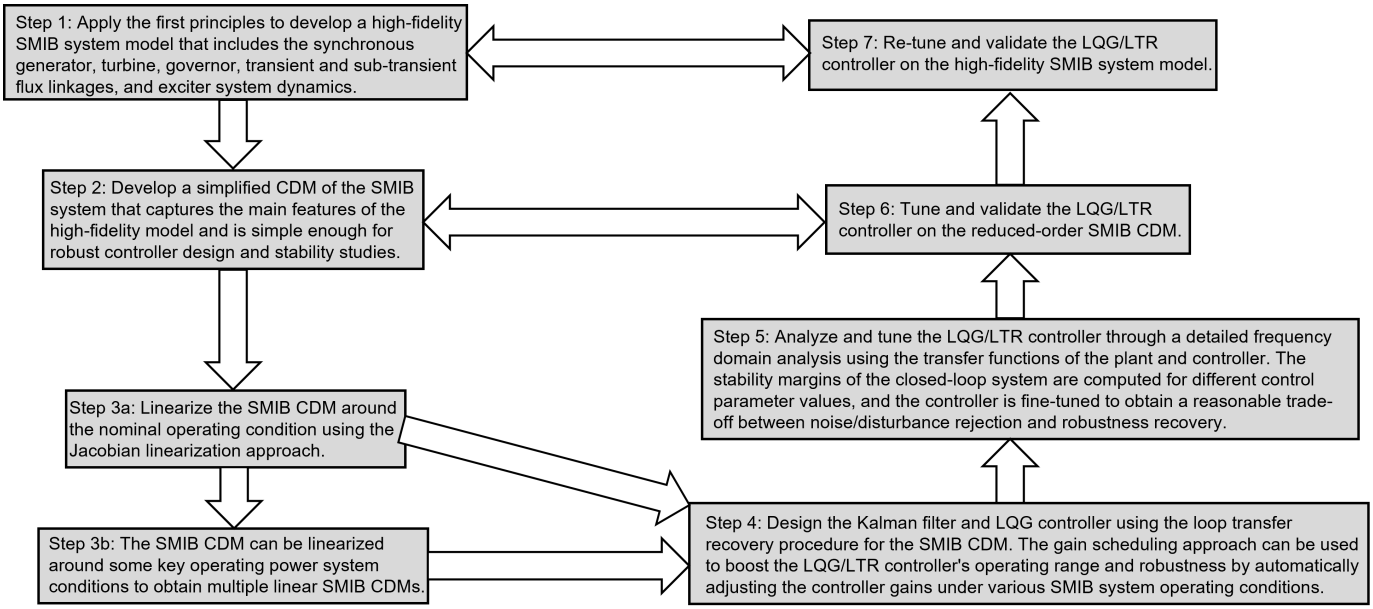

Fig. 2. Framework for robust LQG/LTR controller design for a detailed model of the SMIB system.

in which $x \in \mathbb{R}^5 = [\Delta E'_q, \Delta\omega, \Delta\delta, \Delta T_m, \Delta G_V]^T$, the control input $u \in \mathbb{R}^2 = [\Delta E_{FD}, \Delta u_T]^{\mathrm{T}}$, the output $y \in \mathbb{R}^2 = [\Delta V_t, \Delta\omega]^T$, the system matrices $A \in \mathbb{R}^{5\times5}$, $B \in \mathbb{R}^{5\times2}$, $C \in \mathbb{R}^{2\times5}$, and $D \in \mathbb{R}^{2\times2}$, where Δ is the deviation from the nominal operating condition, i.e., $\Delta E'_q = E'_q - E'_{q0}$, $\Delta\omega = \omega - \omega_0$, $\Delta\delta = \delta - \delta_0$, $\Delta T_m = T_m - T_{m0}$, $\Delta G_V = G_V - G_{V0}$, $\Delta E_{FD} = E_{FD} - E_{FD0}$, and $\Delta u_T = u_T - u_{T0}$. Moreover, d_1 and d_2 represent power system faults, external disturbances, and sudden load fluctuations. Furthermore, v_1 and v_2 are fictitious process and sensor noise inputs employed as design parameters to improve the LQG/LTR controller's robustness in the presence of external disturbances, uncertainties, and plant/model mismatch. In Section V, a three-phase short-circuit fault at the generator terminal, changes in mechanical power input to the generator, and an increase in the machine loading are some of the case studies used to validate the robustness of the LQG/LTR controller in the presence of severe power system faults and disturbances represented by d_1 and d_2. In (12), the system matrices (A, B, C, D) around the operating point (x_0, u_0) are

$$A = \begin{bmatrix} f_{11} & 0 & \frac{\partial f_1}{\partial x_3} & 0 & 0 \\ \frac{\partial f_2}{\partial x_1} & f_{27} & \frac{\partial f_2}{\partial x_3} & f_{28} & 0 \\ 0 & 1 & 0 & 0 & 0 \\ 0 & 0 & 0 & f_{41} & f_{42} \\ 0 & f_{51} & 0 & 0 & f_{52} \end{bmatrix}, \quad B = \begin{bmatrix} g_{11} & 0 \\ 0 & 0 \\ 0 & 0 \\ 0 & 0 \\ 0 & g_{55} \end{bmatrix},$$
$$C = \begin{bmatrix} T_1 & 0 & T_2 & 0 & 0 \\ 0 & 1 & 0 & 0 & 0 \end{bmatrix}, \quad D = \begin{bmatrix} 0 & 0 \\ 0 & 0 \end{bmatrix}, \tag{13}$$

in which $\frac{\partial f_1}{\partial x_3}$, $\frac{\partial f_2}{\partial x_1}$, and $\frac{\partial f_2}{\partial x_3}$ are computed at the operating point x_0, where

$$f_1(x) = f_{11}x_1 + f_{12}\cos(x_3 - \alpha) + f_{13}\sin(x_3 - \alpha),$$
$$f_2(x) = f_{21}x_1^2 + f_{22}x_1\cos(x_3 - \alpha) + f_{28}x_4 + f_{23}x_1\sin(x_3 - \alpha) + f_{24}\sin(x_3 - \alpha)\cos(x_3 - \alpha) + f_{25}\cos^2(x_3 - \alpha) + f_{26}\sin^2(x_3 - \alpha) + f_{27}x_2,$$
$$T_1 = \left(\frac{V_{d0}}{V_{t0}}V_{d1} + \frac{V_{q0}}{V_{t0}}V_{q1} + \frac{V_{q0}}{V_{t0}}\right),$$
$$T_2 = \left(\frac{V_{d0}}{V_{t0}}V_{d3}\cos(\delta_\circ - \alpha) - \frac{V_{d0}}{V_{t0}}V_{d2}\sin(\delta_\circ - \alpha) - \frac{V_{q0}}{V_{t0}}V_{q2}\sin(\delta_\circ - \alpha) + \frac{V_{q0}}{V_{t0}}V_{q3}\cos(\delta_\circ - \alpha)\right).$$

- **Step 2: Kalman filter and LQG controller design using loop transfer recovery**

Intensive simulations revealed the incapability of the Luenberger observer and the LQG controller to reliably estimate the states of the SMIB system's reduced-order CDM. Also, the Luenberger observer-based LQR and LQG controllers are not robust to variations in the operating conditions, unmodeled internal dynamics, uncertainties, and mismatch between the reduced-order CDM and the high-fidelity model of the SMIB system. To address this issue and boost the observer's robustness, we developed a robust LQG controller in which the Kalman filter gains are tuned using the loop transfer recovery (LTR) procedure. A gain adjustment design procedure in the time domain, analogous to loop shaping in the frequency domain, is used to adjust the gains of the Kalman filter [27], [29]. This gain adjustment procedure asymptotically achieves the same loop transfer function as a full-state feedback LQR controller while improving the observer's robustness. The Kalman filter is configured to restore the full-state feedback LQR robustness features at the plant input. The Kalman filter provides estimates of the rotor angle δ and the q-axis voltage

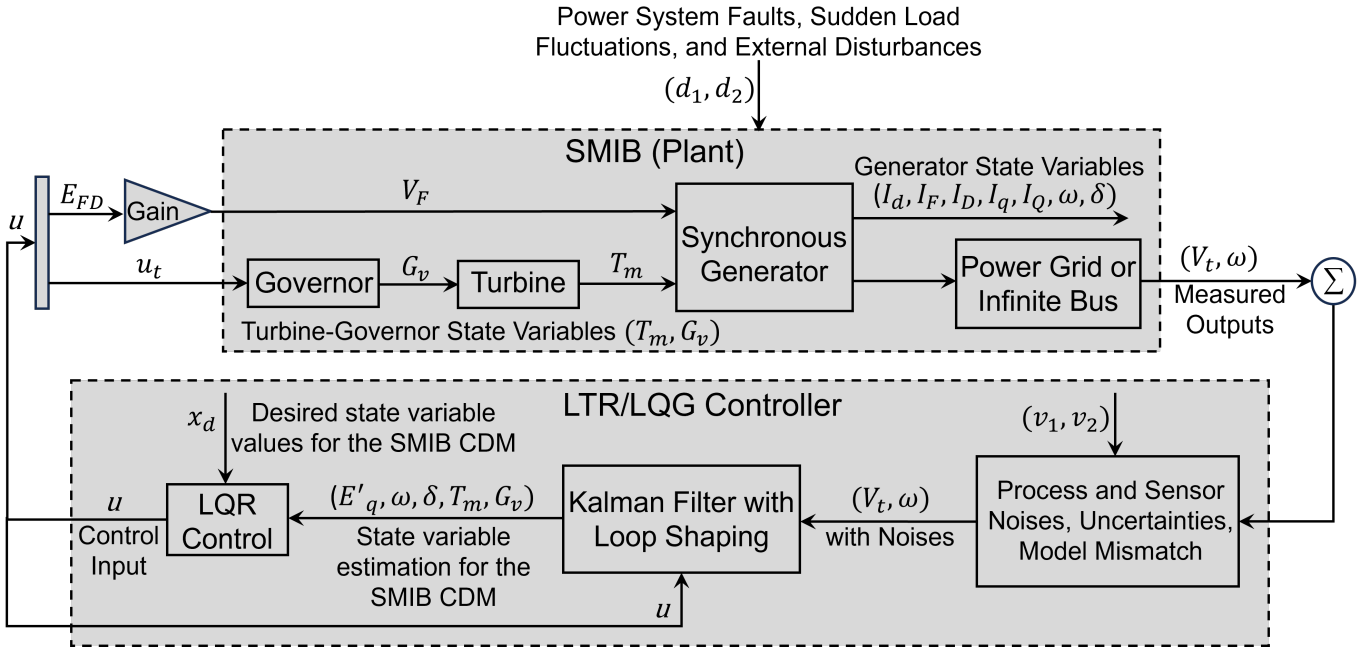

Fig. 3. Schematic of the proposed LTR/LQG control scheme for a detailed model of the SMIB system.

E'_q of the SMIB system that cannot be easily measured using sensors. The Kalman filter that produces an estimate of the state, $\hat{x}$, is of the form

$$\begin{aligned} \dot{\hat{x}} &= A\hat{x} + Bu + H(y - \hat{y}), \\ \hat{y} &= C\hat{x}, \;\; H(q) = \Psi(q)C^T V_2^{-1}, \end{aligned} \tag{14}$$

in which $H(q)$ is the Kalman filter gain parameterized as a function of a scalar variable q, and $\Psi(q)$ is the unique symmetric positive semi-definite solution of the following algebraic matrix Riccati equation

$$A\Psi(q) + \Psi(q)A^T + V_1(q) - \Psi(q)C^T V_2^{-1} C\Psi(q) = 0. \tag{15}$$

The covariance matrices $V_1(q) \in \mathbb{R}^{5\times5}$ and $V_2 \in \mathbb{R}^{2\times2}$, which represent the process and measurement noise intensities associated with the signals v_1 and v_2, respectively, are regarded as design parameters of the Kalman filter. The fictitious noise signals v_1 and v_2 are introduced to take into account the uncertainties, unmodeled dynamics, and differences between the reduced-order CDM and the actual plant of the SMIB system. We select $V_1(q) = V_1^T(q) > 0$ and $V_2 = V_2^T > 0$ with $(A, V_1^{\frac{1}{2}}(q))$ being stabilizable and (C, A) being observable. The design parameter $V_1(q)$ is chosen as follows:

$$V_1(q) = V_{10} + q^2 BVB^T, \tag{16}$$

in which $V_{10} \in \mathbb{R}^{5\times5}$. The diagonal matrices V_{10} and V_2 represent noise intensities appropriate for the nominal high-fidelity SMIB plant model (7), and $V \in \mathbb{R}^{2\times2}$ is a positive definite symmetric matrix. The observer gain for $q = 0$ corresponds to the nominal Kalman filter gain $H(0)$. By substituting (16) into (15) and dividing (15) by q^2, we get

$$\begin{aligned} &A\frac{\Psi(q)}{q^2} + \frac{\Psi(q)}{q^2}A^T + \frac{V_{10}}{q^2} + BVB^T \\ &- \Psi(q)C^T V_2^{-1} C\frac{\Psi(q)}{q^2} = 0. \end{aligned} \tag{17}$$

We know that $\frac{\Psi(q)}{q^2} \to 0$ as $q \to \infty$ whenever the transfer function $C(sI - A)^{-1}B$ has no right half-plane zeros. Therefore, as $q \to \infty$, the gains are seen from (17) to satisfy

$$\begin{aligned} &\Psi(q)C^T V_2^{-1} C\frac{\Psi(q)}{q^2} \to BVB^T, \\ &\text{i.e.,} \;\; \frac{H(q)V_2 H^T(q)}{q^2} \to BVB^T. \end{aligned} \tag{18}$$

Solutions of (18) are of the form $\frac{H(q)}{q} \to BV^{\frac{1}{2}}(V_2^{\frac{1}{2}})^{-1}$, in which $V^{\frac{1}{2}}$ is the square root of V, i.e., $(V^{\frac{1}{2}})^T V^{\frac{1}{2}} = V$, and $V_2^{\frac{1}{2}}$ is the square root of V_2. The above solution is a special case of the ideal Kalman filter gain selection $\frac{H(q)}{q} \to BN$ as $q \to \infty$ for any non-singular matrix N. For the ideal Kalman filter gain scenario, the loop transfer functions for the LQG/LTR and full-state feedback controllers are identical if the Kalman filter dynamics satisfy $H(q)[I + C(sI - A)^{-1}H(q)]^{-1} = B[C(sI - A)^{-1}B]^{-1}$ for all values of the complex variable s [29].

After designing the Kalman filter with the LTR approach, the LQG controller $u = [\Delta E_{FD}, \Delta u_T]^{\mathrm{T}}$ is designed next with optimal control theory using the LQR technique. The separation principle allows us to design the LQG controller gain K independent of the Kalman filter formulation $H(q)$. The LQG problem is to obtain an optimal control law $u(t)$ that minimizes the following cost function:

$$J = \lim_{T\to\infty} \frac{1}{T} E\left[\int_0^T (x^T(t)Qx(t) + u^T(t)Ru(t))dt\right], \tag{19}$$

in which $Q = Q^T \in \mathbb{R}^{5\times5} \geq 0$ is a symmetric positive semi-definite weighting matrix, and $R = R^T \in \mathbb{R}^{2\times2} > 0$ is a symmetric positive definite weighting matrix. The matrices Q and R are diagonal matrices with weights appropriately chosen

for all the state variables and control inputs to obtain the desired system response. The LQG control law is $u = -K\hat{x}$, in which $K = R^{-1}B^TP$, where P is the unique symmetric positive semi-definite solution of the algebraic matrix Riccati equation $A^TP + PA - PBR^{-1}B^TP + Q = 0$, with (A, B) being controllable and (Q, A) being observable.

- **Step 3: Closed-loop stability**

Augmenting the SMIB system model (12) with the Kalman filter dynamics (14), and substituting $u = -K\hat{x}$ in equations (12) and (14), we can write the closed-loop dynamics of the SMIB system as follows:

$$\begin{bmatrix}\dot{x}\\ \dot{\hat{x}}\end{bmatrix} = \begin{bmatrix}A & -BK\\ H(q)C & A - BK - H(q)C\end{bmatrix}\begin{bmatrix}x\\ \hat{x}\end{bmatrix} + \begin{bmatrix}v_1\\ H(q)v_2\end{bmatrix} \tag{20}$$

The LQG/LTR controller with $u = -K\hat{x}$ and the Kalman filter gain $H(q)$ designed using the LTR procedure asymptotically stabilizes the SMIB system model (12) if the closed-loop system dynamics matrix in (20) is Hurwitz, i.e., the eigenvalues of the control $(A - BK)$ and observer $(A - H(q)C)$ matrices are in the left half s-plane. Since the pair (A, B) is controllable and the pair (C, A) is observable, stability of the closed-loop dynamics (20) can be ensured by appropriately designing the control $(A - BK)$ and observer $(A - H(q)C)$ matrices.

To maintain the system's closed-loop stability at every point of the LTR-based Kalman filter adjustment trajectory $H(q)$ with limiting characteristics corresponding to the ideal Kalman filter gain $\frac{H(q)}{q} \to BN$, extra care should be taken while formulating a stable $(A - H(q)C)$ observer dynamics to recover the required robustness at the plant input. The LQG/LTR is a virtual design procedure that uses fictitious noise inputs to represent uncertainties and unmodeled plant dynamics to recover the full-state robustness of minimum phase systems asymptotically at the plant input. At $q = 0$, the Kalman filter will be optimal for the nominally linearized SMIB system (12) with the system noise signals v_1 and v_2 known and modeled precisely. Theoretically, as the value of q increases, the noise rejection ability of the filter decreases, but the closed-loop stability margin of the system increases [29], reaching its maximum at $q = \infty$. Nevertheless, simulations confirm that, for large values of q, the LQG/LTR controller application to the high-fidelity SMIB plant model (7) leads to instability, as a practical implementation only achieves partial recovery. A full recovery at high values of q will deteriorate the nominal performance of the system and render the system unstable. Thus, the choice of q is critical, and it cannot be arbitrarily selected to a large value when applying this design adjustment procedure to the actual plant. Furthermore, the LQG/LTR design technique is appropriate for robust SMIB system control since the open-loop SMIB system is square, minimum phase, controllable, and observable. To achieve a reasonable trade-off between the noise/disturbance rejection, closed-loop stability margin, and nominal performance of the system, the scalar q is appropriately tuned by a detailed frequency domain analysis presented next.

- **Step 4: Frequency response analysis**

The LQG/LTR controller design is analyzed through frequency domain analysis using the linearized MIMO SMIB system model (12). The transfer function of the plant or the SMIB system (12) between the control inputs $[\Delta E_{FD}, \Delta u_T]^{\mathrm{T}}$ and outputs $[\Delta V_t, \Delta\omega]^T$ is

$$N_P(s) = \begin{bmatrix}N_{11}(s) & N_{12}(s)\\ N_{21}(s) & N_{22}(s)\end{bmatrix} = C(sI - A)^{-1}B. \tag{21}$$

In (21), $N_{11}(s)$, $N_{12}(s)$, $N_{21}(s)$, and $N_{22}(s)$ are the individual 5^{th}-order transfer functions between the two control inputs and two outputs, respectively, and take the following polynomial form:

$$\begin{aligned}
N_{11}(s) &= \frac{\eta_1 s^4 + \eta_2 s^3 + \eta_3 s^2 + \eta_4 s + \eta_5}{s^5 + \gamma_1 s^4 + \gamma_2 s^3 + \gamma_3 s^2 + \gamma_4 s + \gamma_5},\\
N_{12}(s) &= \frac{\theta_1 s - \theta_2}{s^5 + \gamma_1 s^4 + \gamma_2 s^3 + \gamma_3 s^2 + \gamma_4 s + \gamma_5},\\
N_{21}(s) &= \frac{-(\lambda_1 s^3 + \lambda_2 s^2 + \lambda_3 s)}{s^5 + \gamma_1 s^4 + \gamma_2 s^3 + \gamma_3 s^2 + \gamma_4 s + \gamma_5},\\
N_{22}(s) &= \frac{\zeta_1 s^2 + \zeta_2 s}{s^5 + \gamma_1 s^4 + \gamma_2 s^3 + \gamma_3 s^2 + \gamma_4 s + \gamma_5},
\end{aligned}$$

in which η_1, η_2, η_3, η_4, η_5, γ_1, γ_2, γ_3, γ_4, γ_5, θ_1, θ_2, λ_1, λ_2, λ_3, ζ_1, and ζ_2 are positive coefficients dependent on the operating conditions of the SMIB system.

Similarly, the LQG/LTR controller gain for the MIMO system can be written in the transfer function form as follows:

$$\begin{aligned}
K_C(s) &= \begin{bmatrix}K_{11}(s) & K_{12}(s)\\ K_{21}(s) & K_{22}(s)\end{bmatrix}\\
&= K(sI - A + BK + H(q)C)^{-1}H(q).
\end{aligned} \tag{22}$$

In (22), $K_{11}(s)$, $K_{12}(s)$, $K_{21}(s)$, and $K_{22}(s)$ are the 5^{th}-order LQG/LTR controller transfer functions and take the following polynomial form:

$$\begin{aligned}
K_{11}(s) &= \frac{\kappa_1 s^4 + \kappa_2 s^3 + \kappa_3 s^2 + \kappa_4 s + \kappa_5}{s^5 + \varepsilon_1 s^4 + \varepsilon_2 s^3 + \varepsilon_3 s^2 + \varepsilon_4 s + \varepsilon_5},\\
K_{12}(s) &= \frac{-(\phi_1 s^4 + \phi_2 s^3 + \phi_3 s^2 + \phi_4 s + \phi_5)}{s^5 + \varepsilon_1 s^4 + \varepsilon_2 s^3 + \varepsilon_3 s^2 + \varepsilon_4 s + \varepsilon_5},\\
K_{21}(s) &= \frac{-\psi_1 s^4 - \psi_2 s^3 + \psi_3 s^2 + \psi_4 s + \psi_5}{s^5 + \varepsilon_1 s^4 + \varepsilon_2 s^3 + \varepsilon_3 s^2 + \varepsilon_4 s + \varepsilon_5},\\
K_{22}(s) &= \frac{\xi_1 s^4 + \xi_2 s^3 + \xi_3 s^2 + \xi_4 s + \xi_5}{s^5 + \varepsilon_1 s^4 + \varepsilon_2 s^3 + \varepsilon_3 s^2 + \varepsilon_4 s + \varepsilon_5},
\end{aligned}$$

in which κ_1, κ_2, κ_3, κ_4, κ_5, ε_1, ε_2, ε_3, ε_4, ε_5, ϕ_1, ϕ_2, ϕ_3, ϕ_4, ϕ_5, ψ_1, ψ_2, ψ_3, ψ_4, ψ_5, ξ_1, ξ_2, ξ_3, ξ_4, and ξ_5 are positive coefficients dependent on the gains of the LQG/LTR controller with $q = 9.0005$ finely tuned for the reduced-order CDM of the SMIB system (10).

The resulting loop transfer function (LTF) of the feedback system is

$$H_{LTF}(s) = K_C(s)N_P(s) = \begin{bmatrix}H_{11}(s) & H_{12}(s)\\ H_{21}(s) & H_{22}(s)\end{bmatrix}, \tag{23}$$

in which

$$\begin{aligned}
H_{11}(s) &= K_{11}(s)N_{11}(s) + K_{12}(s)N_{21}(s),\\
H_{12}(s) &= K_{11}(s)N_{12}(s) + K_{12}(s)N_{22}(s),\\
H_{21}(s) &= K_{21}(s)N_{11}(s) + K_{22}(s)N_{21}(s),\\
H_{22}(s) &= K_{21}(s)N_{12}(s) + K_{22}(s)N_{22}(s),
\end{aligned} \tag{24}$$

$$H_{11}(s) = \frac{\begin{array}{c}(\sigma_1 s^{18} + \sigma_2 s^{17} + \sigma_3 s^{16} + \sigma_4 s^{15} + \sigma_5 s^{14} + \sigma_6 s^{13} + \sigma_7 s^{12} + \sigma_8 s^{11} + \sigma_9 s^{10} + \sigma_{10} s^9 \\ +\sigma_{11} s^8 + \sigma_{12} s^7 + \sigma_{13} s^6 + \sigma_{14} s^5 + \sigma_{15} s^4 + \sigma_{16} s^3 + \sigma_{17} s^2 + \sigma_{18} s + \sigma_{19})\end{array}}{\begin{array}{c}(s^{20} + \rho_1 s^{19} + \rho_2 s^{18} + \rho_3 s^{17} + \rho_4 s^{16} + \rho_5 s^{15} + \rho_6 s^{14} + \rho_7 s^{13} + \rho_8 s^{12} + \rho_9 s^{11} + \rho_{10} s^{10} \\ +\rho_{11} s^9 + \rho_{12} s^8 + \rho_{13} s^7 + \rho_{14} s^6 + \rho_{15} s^5 + \rho_{16} s^4 + \rho_{17} s^3 + \rho_{18} s^2 + \rho_{19} s + \rho_{20})\end{array}}, \tag{25}$$

$$H_{12}(s) = \frac{\begin{array}{c}-(\vartheta_1 s^{16} + \vartheta_2 s^{15} + \vartheta_3 s^{14} + \vartheta_4 s^{13} + \vartheta_5 s^{12} + \vartheta_6 s^{11} + \vartheta_7 s^{10} + \vartheta_8 s^9 + \vartheta_9 s^8 \\ +\vartheta_{10} s^7 + \vartheta_{11} s^6 + \vartheta_{12} s^5 + \vartheta_{13} s^4 + \vartheta_{14} s^3 + \vartheta_{15} s^2 + \vartheta_{16} s + \vartheta_{17})\end{array}}{\begin{array}{c}(s^{20} + \rho_1 s^{19} + \rho_2 s^{18} + \rho_3 s^{17} + \rho_4 s^{16} + \rho_5 s^{15} + \rho_6 s^{14} + \rho_7 s^{13} + \rho_8 s^{12} + \rho_9 s^{11} + \rho_{10} s^{10} \\ +\rho_{11} s^9 + \rho_{12} s^8 + \rho_{13} s^7 + \rho_{14} s^6 + \rho_{15} s^5 + \rho_{16} s^4 + \rho_{17} s^3 + \rho_{18} s^2 + \rho_{19} s + \rho_{20})\end{array}}, \tag{26}$$

$$H_{21}(s) = \frac{\begin{array}{c}-(\varphi_1 s^{18} + \varphi_2 s^{17} + \varphi_3 s^{16} + \varphi_4 s^{15} + \varphi_5 s^{14} + \varphi_6 s^{13} + \varphi_7 s^{12} + \varphi_8 s^{11} + \varphi_9 s^{10} + \varphi_{10} s^9 \\ +\varphi_{11} s^8 + \varphi_{12} s^7 + \varphi_{13} s^6 + \varphi_{14} s^5 + \varphi_{15} s^4 + \varphi_{16} s^3 + \varphi_{17} s^2 - \varphi_{18} s - \varphi_{19})\end{array}}{\begin{array}{c}(s^{20} + \rho_1 s^{19} + \rho_2 s^{18} + \rho_3 s^{17} + \rho_4 s^{16} + \rho_5 s^{15} + \rho_6 s^{14} + \rho_7 s^{13} + \rho_8 s^{12} + \rho_9 s^{11} + \rho_{10} s^{10} \\ +\rho_{11} s^9 + \rho_{12} s^8 + \rho_{13} s^7 + \rho_{14} s^6 + \rho_{15} s^5 + \rho_{16} s^4 + \rho_{17} s^3 + \rho_{18} s^2 + \rho_{19} s + \rho_{20})\end{array}}, \tag{27}$$

$$H_{22}(s) = \frac{\begin{array}{c}(\beta_1 s^{16} + \beta_2 s^{15} + \beta_3 s^{14} + \beta_4 s^{13} + \beta_5 s^{12} + \beta_6 s^{11} + \beta_7 s^{10} + \beta_8 s^9 + \beta_9 s^8 \\ +\beta_{10} s^7 + \beta_{11} s^6 + \beta_{12} s^5 + \beta_{13} s^4 + \beta_{14} s^3 + \beta_{15} s^2 + \beta_{16} s - \beta_{17})\end{array}}{\begin{array}{c}(s^{20} + \rho_1 s^{19} + \rho_2 s^{18} + \rho_3 s^{17} + \rho_4 s^{16} + \rho_5 s^{15} + \rho_6 s^{14} + \rho_7 s^{13} + \rho_8 s^{12} + \rho_9 s^{11} + \rho_{10} s^{10} \\ +\rho_{11} s^9 + \rho_{12} s^8 + \rho_{13} s^7 + \rho_{14} s^6 + \rho_{15} s^5 + \rho_{16} s^4 + \rho_{17} s^3 + \rho_{18} s^2 + \rho_{19} s + \rho_{20})\end{array}}, \tag{28}$$

are 20^{th}-order individual LTFs of the MIMO system as given in equations (25), (26), (27), and (28) in the standard polynomial form. The coefficients $(\sigma_1, \cdots, \sigma_{19})$, $(\rho_1, \cdots, \rho_{20})$, $(\vartheta_1, \cdots, \vartheta_{17})$, $(\varphi_1, \cdots, \varphi_{19})$, and $(\beta_1, \cdots, \beta_{17})$ in equations (25), (26), (27), and (28) are positive constants mathematically computed using the relations given in equation (24). Conversely, the LQG/LTR controller design based on the linearized version of the high-fidelity SMIB system model (7) will result in 9^{th}-order LQG/LTR controller transfer functions and exponentially higher-order LTFs, which will further increase the complexity of the closed-loop system. The problem is even more challenging when multiple LQG/LTR controllers are designed for interconnected multi-machine power systems. Thus, the LQG/LTR design based on the reduced-order linearized CDM (12) of the SMIB system is justified. For maximum robustness recovery of the system at the plant input, the Kalman filter gain $H(q)$ should be designed such that $H_{LTF}(s)$ satisfies $\lim_{q\to\infty} K_C(s)N_P(s) = K(sI - A)^{-1}B$, which corresponds to the ideal Kalman filter gain $H(q) = qBV^{\frac{1}{2}}(V_2^{\frac{1}{2}})^{-1}$.

Figs. 4 and 5 show Bode and Nyquist diagrams of the LTFs H_{11}(s) and H_{22}(s) for q = 0, 9.0005, 100, and the ideal Kalman filter gain $H(q)$ using the LQR/LTR design procedure. The tuning parameters of the Kalman filter are chosen as $V_{10} = I_{5\times5}$, $V = I_{2\times2}$, and $V_2 = I_{2\times2}$. The LQG controller gain K is designed using the LQR technique (19) such that the closed-loop system dynamics matrix in (20) is Hurwitz. Table I documents the gain margins (GMs) (dB) and phase margins (PMs) (deg) of the LTFs H_{11}(s) and H_{22}(s) for various q parameter values depicted in the respective Bode and Nyquist diagrams. Figures 4, 5, and Table I demonstrate that for the LTF H_{11}(s), the GMs are infinite for the ideal $H(q)$, q = 0, and 9.0005; the GM is very low (0.0684 dB) for q = 100; and the PMs range from $69 - 78$ degrees. Also, for the LTF H_{22}(s), the GM of 45.195 dB for q = 9.0005 is significantly higher than the GMs for other q values, and the PMs are infinite for q = 0 and 9.0005. We choose q = 9.0005 for the LQG/LTR controller built for the reduced-order CDM (10) to obtain a reasonable compromise between noise/disturbance rejection and robustness recovery within the frequency range of interest. Also, from the Bode plots in Fig. 4, we can see that at higher frequencies, the plots for $q = 9.0005$ and the ideal $H(q)$ converge or move at similar roll-off rates. The Nyquist diagrams of the LTFs H_{11}(s) (top), H_{22}(s) (middle), and H_{22}(s) zoomed version (bottom) in Fig. 5 show that the Nyquist contours for q = 0, 9.0005, and the ideal $H(q)$ do not encircle the $-1 + j0$ point. However, the Nyquist contours for $q = 100$ encircle the $-1 + j0$ point once. Since the open-loop SMIB system (12) is stable, from the Nyquist stability criteria, we can conclude that the closed-loop SMIB system corresponding to the LTFs H_{11}(s) and H_{22}(s) is unstable for $q = 100$. Thus, we can reaffirm that the closed-loop SMIB system becomes unstable, and the margins approach zero for large values of q. The frequency response analyses of the LTFs $H_{12}(s)$ and $H_{21}(s)$ are excluded for brevity.

TABLE I
FREQUENCY DOMAIN ANALYSIS FOR VARIOUS q PARAMETER VALUES.

LQG/LTR Design	GM (dB) $H_{11}(s)$	PM (deg) $H_{11}(s)$	GM (dB) $H_{22}(s)$	PM (deg) $H_{22}(s)$
$q = 0$	∞	75.616	8.347	∞
$q = 9.0005$	∞	71.793	45.195	∞
$q = 100$	0.0684	77.533	0.4622	69.475
Ideal $H(q)$	∞	69.501	3.561	36.046

- **Step 5: The correlation between the field voltage V_F and excitation field EMF E_{FD} control inputs**

We now provide a mechanism for applying the proposed LQG/LTR controller, designed based on the reduced-order CDM of the SMIB system (10), to the high-fidelity model (7) of the SMIB system. We thus establish the interconnection between the control inputs V_F and E_{FD} for the high-fidelity

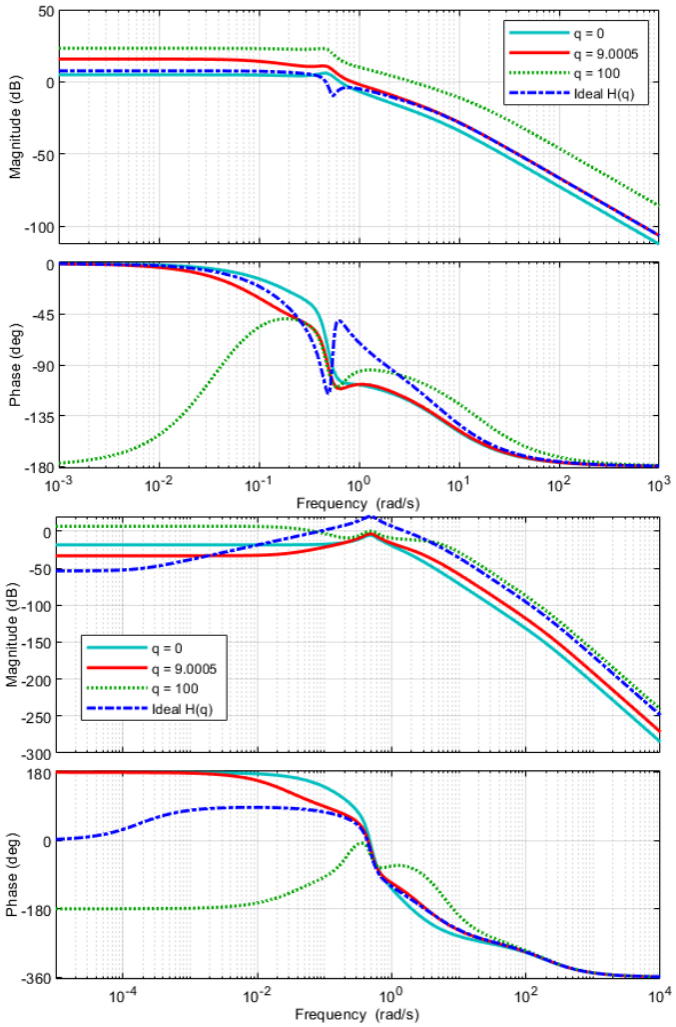

Fig. 4. Bode plots (magnitude and phase responses) of the transfer functions H_{11}(s) (top) and H_{22}(s) (bottom) for various q parameter values.

model and the reduced-order CDM, respectively. One of the distinguishing features of the proposed controller includes the correlation between the control inputs for the two models and its practicality on SMIB models of varying complexities. For the reduced-order CDM (10), the two control inputs are $u = [E_{FD}, u_T]^{\mathrm{T}}$, whereas for the high-fidelity model (7), $u = [V_F, u_T]^{\mathrm{T}}$ is the vector of control inputs. Thus, the proposed LQG/LTR controller cannot be directly applied to the high-fidelity model since the control inputs V_F and E_{FD} are distinct. The field voltage, V_F, is related to the excitation field EMF, E_{FD}, by the following expression:

$$V_F = \left(\frac{r_F}{\omega_R k M_F}\right) E_{FD}. \tag{29}$$

V. Simulation and Comparison

To evaluate the performance of the proposed LQG/LTR control approach, we first consider the following case study:

- Case 1: A three-phase short-circuit fault at the generator terminal for the reduced-order SMIB CDM (10)

Next, the performance of the LQG/LTR controller is compared with three nonlinear controllers: the exact feedback linearization control (EFLC) [19]–[22], the integral exact feedback linearization control (IEFLC) [22], and the partial feedback linearization control (PFLC) [12]–[18], on the reduced-order CDM of the SMIB system (10) under different scenarios through the following two case studies:

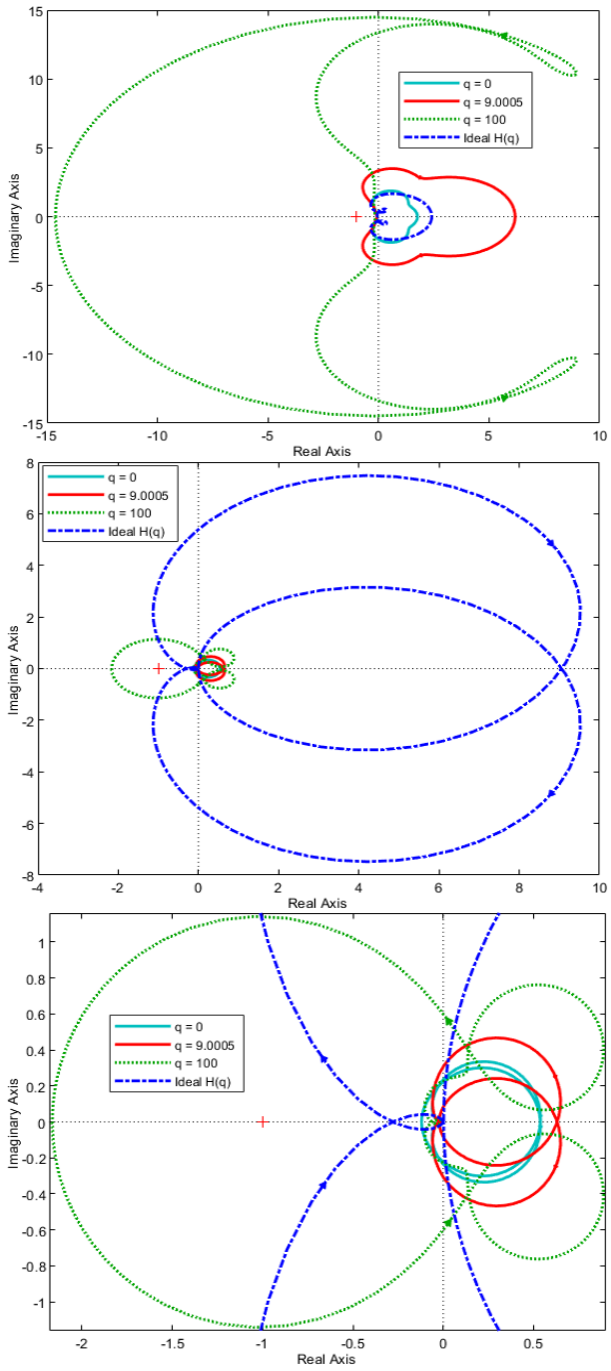

Fig. 5. Nyquist diagrams of the transfer functions H_{11}(s) (top), H_{22}(s) (middle), and H_{22}(s) zoomed version (bottom) for various q parameter values.

- Case 2: Nominal operating condition (Operating Point I) for the SMIB CDM
- Case 3: Changes in mechanical power input to the generator for the SMIB CDM

The EFLC technique used for the comparison in this

manuscript employs the rotor angle δ and the turbine torque T_m as the system outputs. In [21], an observer-based EFLC approach is presented for excitation controller design in an interconnected power system. The IEFLC method [22] enhances the EFLC strategy with integral action on the generator and turbine-governor subsystems to reduce the steady-state error. The PFLC approach used for the comparison in this article utilizes the speed ω and the turbine torque T_m as the system outputs. The PFLC method is employed as the baseline controller in several SMIB and multi-machine power system studies [12]–[18]. It is important to note that the EFLC [19]–[21] and PFLC [12]–[17] approaches reported in the literature do not use the turbine torque T_m as the second output since they do not consider the turbine-governor dynamics.

Finally, the following two operating scenarios are used to assess the effectiveness of the suggested LQG/LTR and nonlinear controllers on the high-fidelity model of the SMIB system (7), which is regarded as the plant model:

- Case 4: Nominal operating condition (Operating Point I) for the high-fidelity SMIB plant model
- Case 5: Increase in the machine loading (Operating Point II) for the high-fidelity SMIB plant model

The ratings and parameters of the synchronous generator used in this study are given in Example 4.1 of [31]. The parameters of the high-fidelity SMIB power system model in the p.u. system are: $L_d = 1.70$, $L_F = 1.65$, $L_D = 1.605$, $L_q = 1.64$, $L_Q = 1.526$, $kM_F = 1.55$, $kM_D = 1.55$, $M_R = 1.55$, $kM_Q = 1.49$, $r = 0.001096$, $r_F = 0.000742$, $r_D = 0.0131$, $r_Q = 0.0540$, $H = 2.37$ s, $R_e = 0.02$, $L_e = 0.4$, $D = 0$, $\omega_0 = 376.99$ rad, $K_T = 1$, $K_G = 1$, $\tau_T = 0.5$, $\tau_G = 0.2$, $R_T = 20$, $k = \sqrt{3/2}$, $L'_d = 0.245$, $\tau'_{d0} = 5.9$, $\tau_j = 4.74$, $V_\infty = 1$, and $\alpha = 3.5598°$. Similarly, the parameters of the reduced-order SMIB system model in the p.u. system are: $V_{d1} = -0.0249$, $V_{d2} = 0.0249$, $V_{d3} = -0.8037$, $V_{q1} = -0.3797$, $V_{q2} = 0.3797$, $V_{q3} = 0.0037$, $f_{11} = -0.5517$, $f_{12} = 0.3822$, $f_{13} = 0.0037$, $f_{21} = -0.0101$, $f_{22} = 0.0171$, $f_{23} = -0.3269$, $f_{24} = 0.2235$, $f_{25} = -0.0069$, $f_{26} = 0.0022$, $f_{27} = 0$, $f_{28} = 0.2110$, $f_{41} = -2$, $f_{42} = 2$, $f_{51} = -0.2500$, $f_{52} = -5$, $g_{11} = 0.1695$, and $g_{55} = 5$. To ensure realistic control inputs for a practical SMIB power system, the physical limits of the excitation field voltage of the generator are $E_{FD\max} = 5$ p.u. and $E_{FD\min} = -5$ p.u., which match the physical limits of the IEEE Type II and IEEE Type AC4A excitation systems [14], [23]. Also, the physical limits of the turbine valve gate opening are $G_{V\max} = 1.2$ p.u. and $G_{V\min} = 0$ p.u.

The steady-state operating conditions of the SMIB system depend on the parameters of the synchronous generator, turbine-governor system, transmission line, and machine loading. The two different operating conditions at which the controllers are validated on the high-fidelity SMIB plant model for case studies 4 and 5 are given in Table II [31]. At these operating conditions, the EFLC, IEFLC, PFLC, and LQG/LTR control methods are thoroughly compared in terms of performance. The nonlinear and LQG/LTR controllers are constructed using the reduced-order nonlinear CDM (10) and the linear CDM (12) linearized about the nominal operating condition (Operating Point I), respectively. At Operating Point I, the machine loading or the real power P generated by the synchronous generator is 1.0 p.u. at 0.85 lagging power factor ($\cos\phi$) conditions. The real power $P = V_t I_a \cos\phi$ produced by the synchronous generator increases to 1.3466 p.u. as the power factor ($\cos\phi$) decreases to 0.652 with an increase in the machine loading at Operating Point II. Furthermore, the stator current $I_{a0} = 1.0037$ p.u. of the synchronous generator at Operating Point I increases to 1.4764 p.u. at Operating Point II when the load on the synchronous generator is increased. Thus, the operating conditions are varied by varying the machine loading, i.e., by increasing or decreasing the load on the generator.

TABLE II
OPERATING POINTS OF THE SMIB SYSTEM

Variables (p.u.)	Nominal Operating Condition (Operating Point I)	Increase in the Machine Loading (Operating Point II)
I_{d0}	-0.9185	-1.4281
I_{F0}	1.6315	2.37786
I_{D0}	-4.6204×10^{-6}	0
I_{q0}	0.4047	0.37472
I_{Q0}	5.9539×10^{-5}	0
ω_0	1.0	1.0
δ_0	1.0	0.88676
T_{m0}	1.0012	1.34899
G_{V0}	1.0012	1.34899
V_{q0}	0.9670	1.2575
V_{d0}	-0.6628	-0.6130
V_{t0}	1.17233	1.39899
I_{a0}	1.0037	1.4764
V_∞	1.0	1.0
α	3.5598°	3.5598°
E'_{q0}	1.1925	1.6078
τ'_{d0}	5.90	5.90
P	1.0	1.3466
$\cos\phi$	0.85	0.652

- **Case 1: A three-phase short-circuit fault at the generator terminal for the SMIB CDM**

In this case study, the most severe fault in power systems is considered, i.e., a three-phase short-circuit fault is applied at the terminal of the synchronous generator. The following fault sequence is considered to evaluate the performance of the proposed LQG/LTR controller:

- The three-phase short-circuit fault occurs at $t = 50$ s.
- The fault is cleared at $t = 50.2$ s.

Figs. 6 and 7 show the system response plots for this case study. During the faulted period from $t = 50$ s to $t = 50.2$ s, the generator does not supply any power, and thus, the terminal voltage V_t is zero, as seen in Fig. 6 (top). For the LQG/LTR controller, the terminal voltage V_t returns to its pre-fault steady-state value after the fault clears at $t = 50.2$ s. The synchronous generator operates at a synchronous speed or angular velocity ω of 1 p.u. during the pre-fault normal operating condition, i.e., until $t = 50$ s, as seen in Fig. 6 (middle). However, the speed exhibits some undershoots and overshoots for the LQG/LTR controller when the fault occurs at $t = 50$ s and after it clears at $t = 50.2$ s. The rotor angle δ displays similar characteristics, as shown in Fig. 6

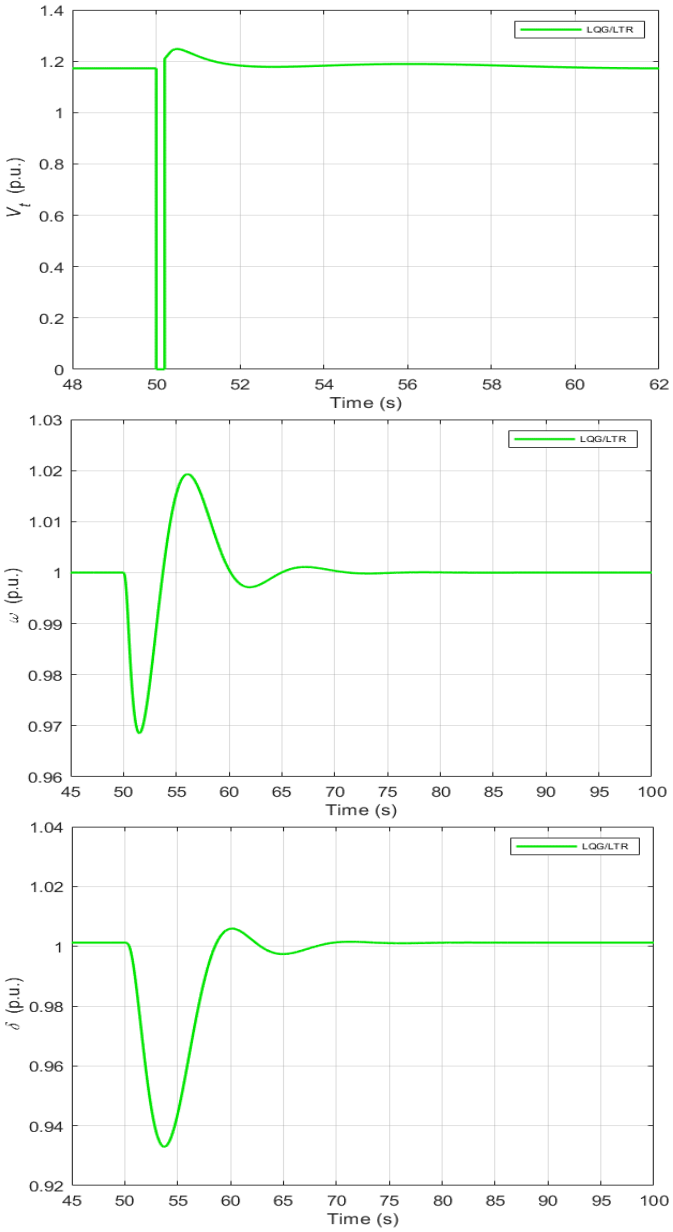

Fig. 6. Terminal voltage V_t (top), speed ω (middle), and rotor angle δ (bottom) response plots for the LQG/LTR controller applied to the reduced-order SMIB CDM when a three-phase short-circuit fault is applied at the generator terminal.

(bottom). For better resolution of the impact of the fault on V_t, it is not on the same time scale as ω and δ in Fig. 6. Fig. 7 shows magnified plots of the excitation field EMF E_{FD} (top) and turbine valve control u_T (bottom) for the LQG/LTR controller. When the fault occurs at $t = 50$ s, the LQG/LTR controller reaches the maximum physical limit (± 5 p.u.) of the generator's excitation field EMF E_{FD} and then returns to its pre-fault steady-state value. Also, the turbine valve control u_T exhibits high-frequency oscillations for the LQG/LTR technique around the time intervals when the fault is initiated and cleared.

The LQG/LTR technique stabilizes the SMIB system in the presence of a three-phase short-circuit fault at the generator

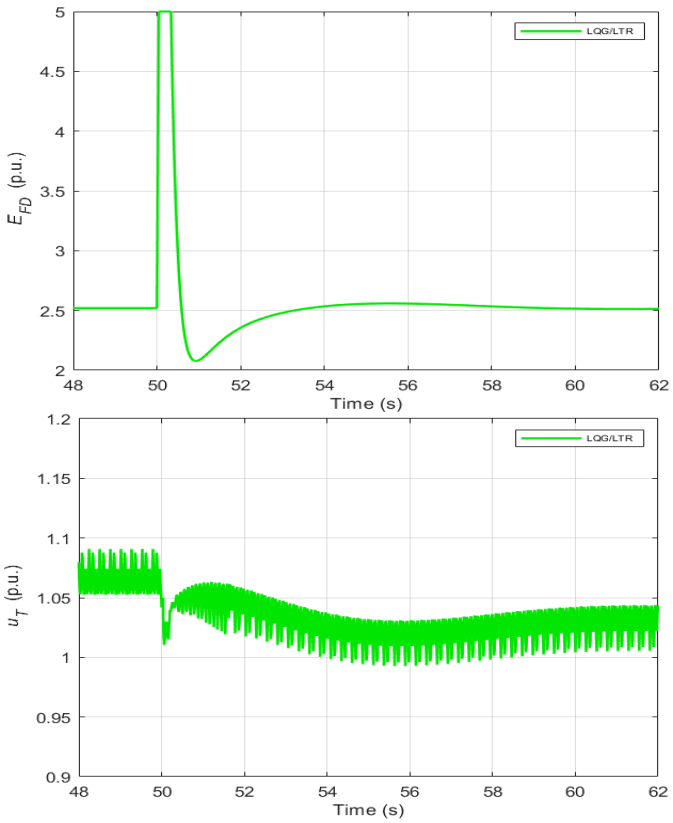

Fig. 7. Excitation field EMF E_{FD} (top) and turbine valve control u_T (bottom) magnified response plots for the LQG/LTR controller applied to the reduced-order SMIB CDM when a three-phase short-circuit fault is applied at the generator terminal.

terminal, with oscillations in the terminal voltage V_t, speed ω, and rotor angle δ responses before they settle to their post-fault steady-state values, respectively. Utilizing the speed ω as the system output for the Kalman filter and LQG/LTR controller design provides more damping into the system compared to the DFLC [7]–[11], EFLC [19]–[22], and IEFLC [22] nonlinear strategies. Therefore, the LQG/LTR controller can ensure transient stability of the speed ω and rotor angle δ and attain post-fault steady-state terminal voltage V_t within a few seconds of the faults. The simulation findings for Case 1 demonstrate that the LQG/LTR method can achieve and maintain the transient stability of the system during a severe power system fault.

- **Case 2: Nominal operating condition (Operating Point I) for the SMIB CDM**

The LQG/LTR, EFLC, IEFLC, and PFLC control techniques are next validated on the reduced-order SMIB CDM (10) at the nominal operating condition. Fig. 8 shows the system response plots for the controllers applied to the reduced-order SMIB CDM at Operating Point I. The simulation results show that for the LQG/LTR, EFLC, and IEFLC controllers, the outputs V_t, ω, δ, and T_m achieve their desired steady-state values of 1.17233, 1.0, 1.0, and 1.0012 p.u., respectively. Whereas, for the PFLC strategy, which only partially linearizes the reduced-order SMIB CDM, a steady-state error is observed in the terminal voltage V_t and rotor angle δ, while

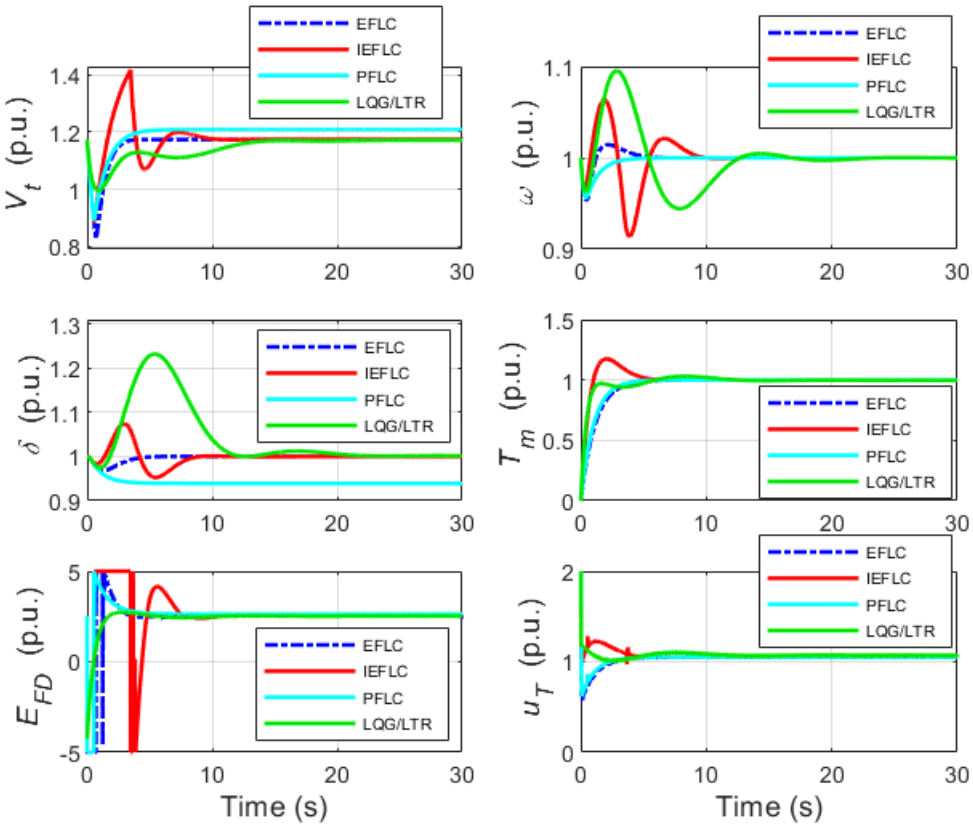

Fig. 8. System response plots (V_t, ω, δ, T_m, E_{FD}, u_T) for the EFLC, IEFLC, PFLC, and LQG/LTR controllers applied to the reduced-order SMIB CDM at Operating Point I.

the speed ω and turbine torque T_m settle to their desired steady-state values. The steady-state equilibrium of the control inputs, $E_{FD(ss)}$ and $u_{T(ss)}$, can be calculated analytically by substituting the steady-state equilibrium values of the state variables x at Operating Point I in the differential equation, $\dot{x} = f(x) + g(x)u = 0$, and solving for the control inputs. A closer inspection of Fig. 8 indicates that the control inputs, E_{FD} and u_T, settle to their desired steady-state values of 2.529 p.u. and 1.0512 p.u., respectively, which conforms with the analytical results. The EFLC and PFLC approaches yield fewer oscillations and smaller peak overshoots of the outputs V_t, ω, δ, and T_m compared to the IEFLC and LQG/LTR controllers. The EFLC outperforms the other controllers in this case study as it precisely linearizes the reduced-order SMIB CDM using the rotor angle δ as the system output for the nonlinear coordinate transformation. Furthermore, the EFLC, IEFLC, and PFLC controllers hit the maximum physical limit (± 5 p.u.) of the generator's excitation field EMF E_{FD}. In contrast, the LQG/LTR excitation field EMF E_{FD} remains well within the physical limits.

- **Case 3: Changes in mechanical power input to the generator for the SMIB CDM**

The generator's output power varies with the system load, which in turn affects the mechanical power input to the generator through the turbine governor action, adjusting the power output to match the load precisely. The mechanical power input to the generator P_m, which is the turbine's output, is numerically equal to the mechanical torque output of the turbine T_m in the p.u. system. In this case study, P_m is held constant at a value of 1 p.u., which is close to the nominal operating condition (Operating Point I), till $t = 25$ s. The mechanical power input to the generator P_m is increased by 10 percent from 1 p.u. to 1.1 p.u. for 25 s, i.e., from $t = 25$ s to $t = 50$ s. Next, P_m is lowered back to 1 p.u. for 25 s, i.e., from $t = 50$ s to $t = 75$ s. Finally, P_m is reduced by 10 percent from 1 p.u. to 0.9 p.u. for 25 s, i.e., from $t = 75$ s to $t = 100$ s. This case study can be summarized as follows in the p.u. system:

$$P_m = T_m = \begin{cases} 1, & 0 \text{ s} \leq t < 25 \text{ s}, \\ 1.1, & 25 \text{ s} \leq t < 50 \text{ s}, \\ 1, & 50 \text{ s} \leq t < 75 \text{ s}, \\ 0.9, & 75 \text{ s} \leq t \leq 100 \text{ s}. \end{cases} \tag{30}$$

Figs. 9 and 10 show the system response plots for this case study. Fig. 9 (top) shows the terminal voltage V_t response to variations in the mechanical power input P_m for the LQG/LTR, EFLC, IEFLC, and PFLC controllers. The plots show that the EFLC, IEFLC, and PFLC controllers undergo step changes in the terminal voltage V_t and settle to new operating points when the mechanical power input P_m is increased ($t = 25$ s to $t = 50$ s) or decreased ($t = 75$ s to $t = 100$ s) from its nominal operating value of 1 p.u. Moreover, the PFLC technique exhibits a steady-state error or an offset in the terminal voltage V_t. However, the terminal

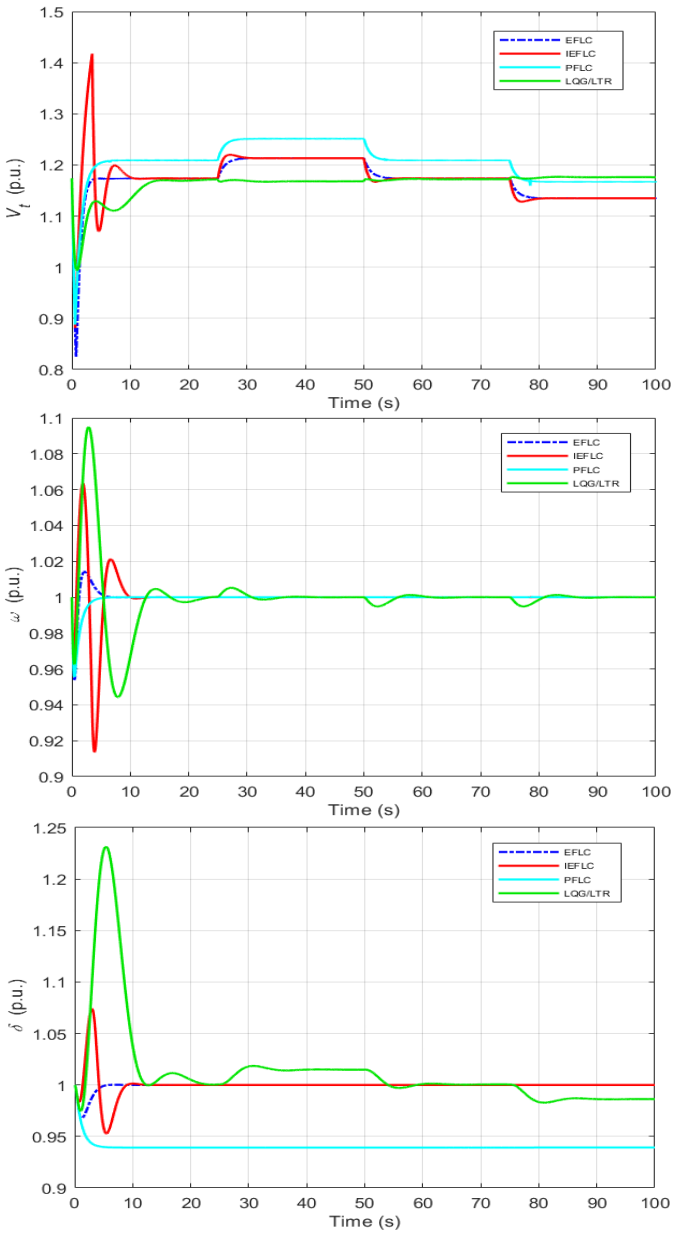

Fig. 9. Terminal voltage V_t (top), speed ω (middle), and rotor angle δ (bottom) response plots for the EFLC, IEFLC, PFLC, and LQG/LTR controllers applied to the reduced-order SMIB CDM when the mechanical power input to the generator is changed.

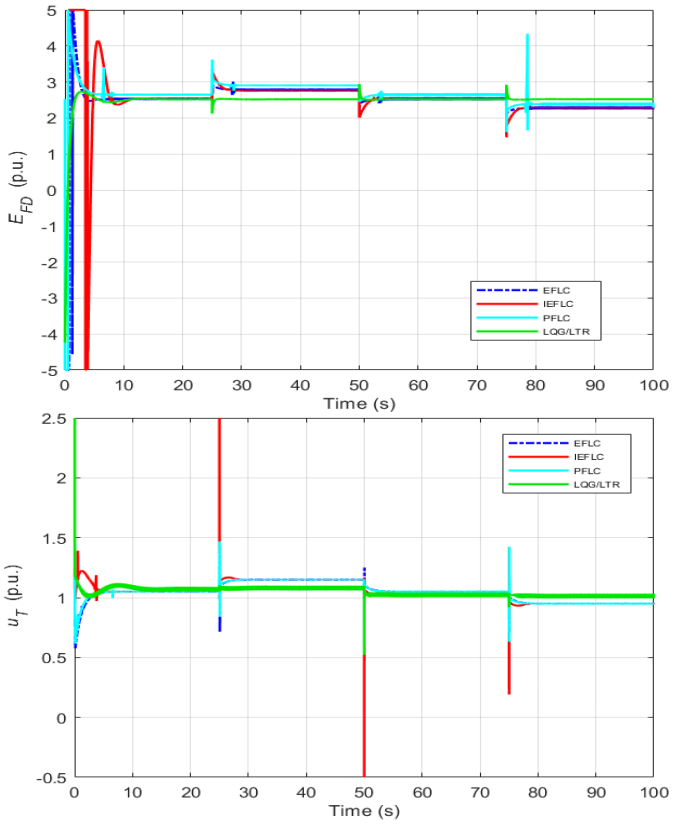

Fig. 10. Excitation field EMF E_{FD} (top) and turbine valve control u_T (bottom) response plots for the EFLC, IEFLC, PFLC, and LQG/LTR controllers applied to the reduced-order SMIB CDM when the mechanical power input to the generator is changed.

voltage V_t for the LQG/LTR approach remains stable after a brief transient period in response to changes in P_m. It settles back near its nominal steady-state operating point. The speed ω response plots in Fig. 9 (middle) for the four controllers reveal that the speed exhibits more undershoots and overshoots before settling to its nominal operating value of 1 p.u. for the LQG/LTR controller than the EFLC, IEFLC, and PFLC methods when P_m is changed from its nominal operating value. Fig. 9 (bottom) shows that the rotor angle δ for the LQG/LTR strategy experiences step changes and settles to new operating points when the mechanical power input P_m is varied from its nominal operating value. However, the rotor angle δ remains stable at its original steady-state equilibrium point for the EFLC and IEFLC techniques. Moreover, the PFLC technique exhibits a steady-state error in the rotor angle δ.

The three controllers' distinct system outputs can explain the step deviations in terminal voltage V_t for the EFLC, IEFLC, and PFLC techniques and the step changes in rotor angle δ for the LQG/LTR approach. The LQG/LTR methodology utilizes V_t and ω as the outputs and their associated reference values. In contrast, the EFLC and IEFLC techniques use δ and T_m, and the PFLC approach uses ω and T_m as the outputs and their corresponding reference values, respectively. Furthermore, the generator's output power will increase or decrease as P_m rises or falls for the LQG/LTR method. As the load remains constant, the surplus or deficiency between the power generated and the load will be satisfied by increasing or reducing the speed of the rotating mass of the generator, resulting in the rotor angle δ stepping up or down and settling to a higher or lower equilibrium point for the LQG/LTR approach. The step changes in terminal voltage V_t to new operating points as P_m increases or decreases for the EFLC, IEFLC, and PFLC can be explained similarly.

Fig. 10 shows plots of the excitation field EMF E_{FD} (top) and turbine valve control u_T (bottom) for the four controllers when the mechanical power input to the generator is changed. These figures illustrate that the IEFLC technique exhibits the largest step changes and deviations from the nominal operating

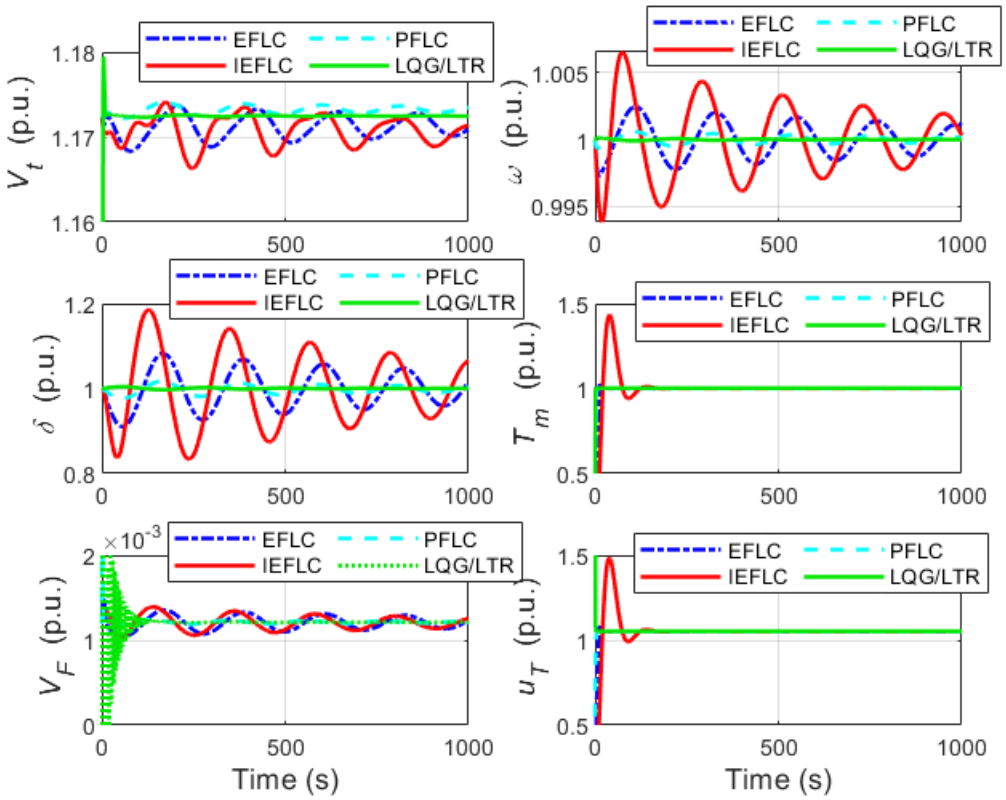

Fig. 11. System response plots (V_t, ω, δ, T_m, V_F, u_T) for the EFLC, IEFLC, PFLC, and LQG/LTR controllers applied to the high-fidelity SMIB power system plant model at Operating Point I.

condition for the control inputs in response to changes in the mechanical power input, followed by the PFLC and EFLC approaches and finally, the LQG/LTR strategy in the decreasing order of fluctuations.

- **Case 4: Nominal operating condition (Operating Point I) for the high-fidelity SMIB plant model**
- **Case 5: Increase in the machine loading (Operating Point II) for the high-fidelity SMIB plant model**

The four controllers' performances are validated and compared on a high-fidelity SMIB power system plant model at Operating Points I and II in case studies 4 and 5, respectively. The gains of the suggested controllers tuned for the reduced-order CDM are re-tuned for optimal performance on the high-fidelity plant model. Moreover, the respective controller gains are unchanged for both Operating Points I and II, except for the PFLC controller. The PFLC gains tuned for Operating Point I had to be re-tuned for Operating Point II to avoid loss of stability and increase the robustness of the PFLC. The LQG/LTR controller gains for the high-fidelity plant model are selected as follows: q = 5.25, $V_{10} = I_{5\times5}$, $V = I_{2\times2}$, $V_2 = 0.65I_{2\times2}$, and the controller gain matrix $K = \begin{bmatrix} 87.3944 & -216.768 & -60.795 & -13.435 & -0.0618 \\ -1.8244 & 98.065 & 17.7303 & 42.1399 & 85.8027 \end{bmatrix}$. Next, after exact linearization of the SMIB CDM, the EFLC controller gains are designed using the LQR technique to obtain $K_G = \begin{bmatrix} 0.09129 & 0.42015 & 0.92121 \end{bmatrix}$ and $K_T = \begin{bmatrix} 0.09129 & 0.43693 \end{bmatrix}$, in which K_G and K_T are the controller gains for the decoupled generator and turbine-governor subsystems, respectively. Furthermore, after integral augmentation of the decoupled generator and turbine-governor subsystems, the IEFLC controller gains derived using the LQR technique are as follows: $\tilde{K}_G = \begin{bmatrix} 0.00733 & 0.06795 & 0.36864 & 0.00039 \end{bmatrix}$ and $\tilde{K}_T = \begin{bmatrix} 0.01077 & 0.14674 & 0.00039 \end{bmatrix}$, in which $\tilde{K}_G$ and $\tilde{K}_T$ are the controller gains for the augmented generator and turbine-governor subsystems, respectively. Finally, after partial linearization of the SMIB CDM, the PFLC controller gain matrix is designed using the LQR technique to obtain $K = \begin{bmatrix} 5.00 & 5.9161 & 0.00 & 0.00 \\ 0.00 & 0.00 & 5.00 & 5.9161 \end{bmatrix}$ at Operating Point I and $K = \begin{bmatrix} 0.006455 & 0.1138 & 0.00 & 0.00 \\ 0.00 & 0.00 & 0.006455 & 0.1138 \end{bmatrix}$ at Operating Point II.

Figs. 11 and 12 show the system response plots for the EFLC, IEFLC, PFLC, and LQG/LTR controllers applied to the high-fidelity SMIB power system plant model at Operating Points I and II, respectively. Also, Table III shows the qualitative and quantitative comparison of the transient and steady-state responses of the control strategies at Operating Points I and II. Figs. 11 and 12 show that V_t, ω, δ, and T_m oscillate about their respective steady-state values at the two operating conditions for the four controllers, in which the oscillations decay with time. A closer examination of Fig. 11 shows that the generator terminal voltage V_t oscillates about a steady-state value of 1.17113, 1.17, 1.17328, and 1.17246 p.u. for the EFLC, IEFLC, PFLC, and LQG/LTR controllers,

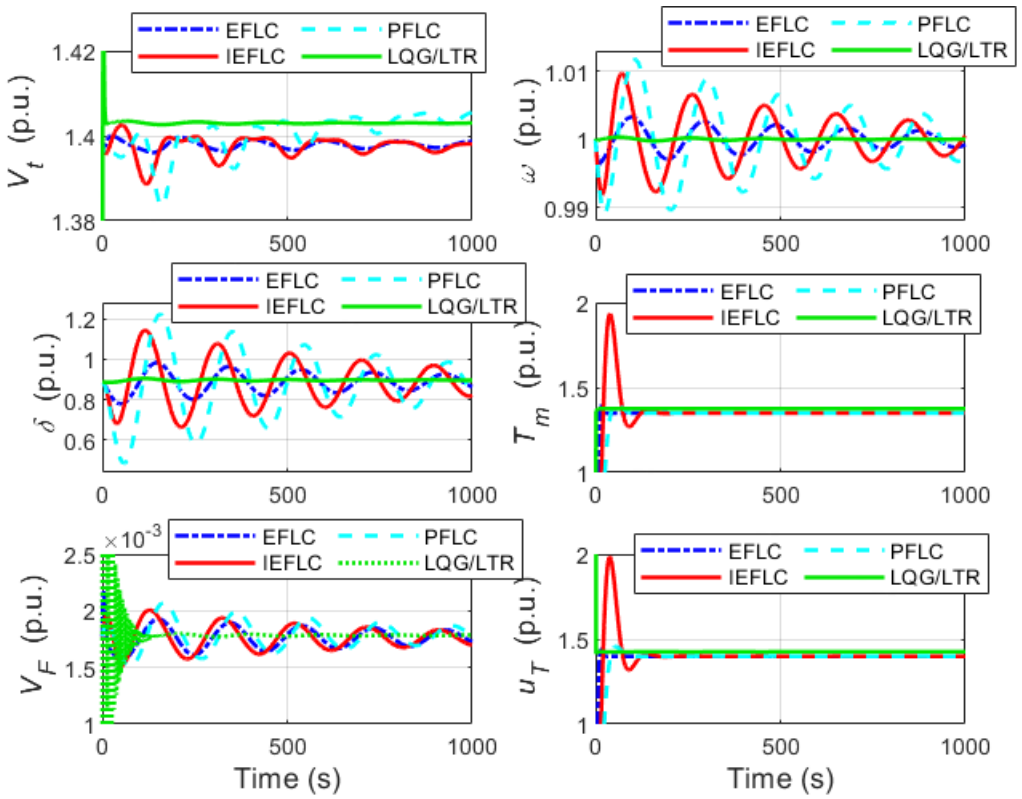

Fig. 12. System response plots (V_t, ω, δ, T_m, V_F, u_T) for the EFLC, IEFLC, PFLC, and LQG/LTR controllers applied to the high-fidelity SMIB power system plant model at Operating Point II.

TABLE III
TRANSIENT AND STEADY-STATE RESPONSE OF DIFFERENT CONTROLLERS AT OPERATING POINTS (OP) I AND II

Control Strategy	Transient Response	Convergence Rate	Steady-State Error at Operating Point I		Steady-State Error at Operating Point II	
			Terminal Voltage V_t	Rotor Angle δ	Terminal Voltage V_t	Rotor Angle δ
EFLC	Good	Medium	0.00120	≈ 0	0.00129	0.00076
IEFLC	Fair	Slow	0.00233	≈ 0	0.00194	0.00684
PFLC	Better (OP I) Fair (OP II)	Fast Slowest	0.00095	0	0.00513	0.01708
LQG/LTR	Best	Fastest	0.00013	0	0.00401	0.00854

respectively, which deviates from the desired steady-state value of 1.17233 p.u. at Operating Point I. Similarly, a closer view of Fig. 12 depicts that the generator terminal voltage V_t oscillates about a steady-state value of 1.3977, 1.39705, 1.40412, and 1.403 p.u. for the EFLC, IEFLC, PFLC, and LQG/LTR controllers, respectively, which deviates from the desired steady-state value of 1.39899 p.u. at Operating Point II. The angular velocity ω attains its desired steady-state value of 1.0 p.u. at both operating points for the LQG/LTR controller. Moreover, the rotor angle δ settles to its desired steady-state value of 1.0 p.u. at Operating Point I for the LQG/LTR and PFLC controllers. However, oscillations in ω and δ about 1.0 p.u. at Operating Point I are seen for the EFLC and IEFLC controllers. Increasing the load on the synchronous generator to 1.3466 p.u. at Operating Point II results in a steady-state error in the rotor angle δ for all four controllers, as shown in Table III. A closer look at Fig. 12 reveals that the rotor angle δ oscillates about a steady-state value of 0.886, 0.8936, 0.86968, and 0.8953 p.u. for the EFLC, IEFLC, PFLC, and LQG/LTR controllers, respectively, which deviates from the desired steady-state value of 0.88676 p.u. at Operating Point II. The generator excitation voltage V_F settles to its steady-state values of 0.00121 p.u. and 0.00176 p.u. at Operating Points I and II, respectively, for the LQG/LTR controller. However, oscillations in V_F are observed at Operating Points I and II for the EFLC, IEFLC, and PFLC controllers. The mechanical torque T_m and the turbine valve control u_T settle to their steady-state values of 1.0012 p.u. and 1.0512 p.u., respectively, at Operating Point I for the four controllers, whereas small oscillations about the steady-state values are observed for all four controllers as the machine loading increases at Operating Point II. The IEFLC exhibits the highest overshoots and undershoots in T_m and u_T at both operating conditions.

The simulation results for case studies 4 and 5 reveal that

the LQG/LTR controller exhibits substantially less oscillatory behavior and faster convergence rates than the EFLC, IEFLC, and PFLC control approaches, in which the oscillations persist for longer periods with higher amplitudes. For the PFLC technique, the oscillations at Operating Point II are significantly higher than those at Operating Point I, even though the controller is re-tuned at Operating Point II for better performance and stability. We also verified through simulations that the PFLC goes unstable at Operating Point II if the gains of Operating Point I are used without fine-tuning. The validation results highlight the limitations of the PFLC methods [12]–[18] in terms of robustness and transient stability enhancement under different operating scenarios and load variations. The IEFLC controller exhibits the highest oscillatory behavior, followed by the EFLC and PFLC approaches in descending order at Operating Point I. Moreover, the PFLC controller manifests the highest oscillations, followed by the IEFLC and EFLC strategies in decreasing order at Operating Point II. Furthermore, the generator terminal voltage V_t exhibits fewer oscillations than the angular velocity ω and rotor angle δ, as depicted in Figs. 11 and 12. The LQG/LTR technique outperforms the EFLC [19]–[22], IEFLC [22], and PFLC [12]–[18] strategies in stabilizing the angular velocity ω and rotor angle δ under different operating conditions.

The qualitative comparative analysis of the controllers' transient responses is summarized in Table III, based on the findings of case studies 4 and 5. Furthermore, Table III indicates that the steady-state error of the terminal voltage V_t is lowest for the LQG/LTR controller, followed by the PFLC and EFLC in ascending order, and highest for the IEFLC at Operating Point I. However, the steady-state errors of the terminal voltage V_t and rotor angle δ are highest for the PFLC controller, followed by the LQG/LTR and IEFLC in descending order, and lowest for the EFLC method at Operating Point II. The EFLC, IEFLC, and PFLC controllers perform less effectively when applied to the high-fidelity plant model since the nonlinear control techniques are model-based and necessitate accurate knowledge of system nonlinearities while also being sensitive to noise and disturbances. Additionally, the plant model differs from the reduced-order CDM utilized for the controller design. Consequently, the EFLC, IEFLC, and PFLC controllers do not effectively negate the nonlinearities and coupling between the electrical and mechanical dynamics in the SMIB plant model. In contrast, the LQG/LTR technique demonstrates superior robustness over various operating conditions, including severe power system faults and load fluctuations. Moreover, the LQG/LTR approach remains unaffected by the mismatch between the reduced-order CDM and the high-fidelity plant model. Overall, the performance of the LQG/LTR controller is comparable to that of the full-state LQR under various SMIB system operating conditions, achieving sufficient robustness recovery at the plant input as the LQG/LTR controller's loop transfer function converges towards the full-state LQR loop transfer function. The parameter q, Kalman filter gain $H(q)$, and covariance matrices of the LQG/LTR controller can be finely tuned to balance robustness and closed-loop stability margins effectively.

VI. Conclusion

This study presents a systematic framework for designing and validating a robust LQG/LTR controller for an SMIB system by utilizing a high-fidelity plant model for validation and a reduced-order CDM for controller synthesis. The LQG/LTR controller employs an enhanced Kalman filter with loop shaping to estimate the rotor angle, q-axis voltage, and other unmeasurable SMIB system states alongside LQR control for optimal closed-loop performance. The Kalman filter gains are tuned using the LTR procedure combined with a comprehensive frequency domain analysis to recover the robustness features of the full-state feedback LQR at the plant input while achieving a reasonable balance between noise/disturbance rejection, closed-loop stability margin, and nominal system performance. Finally, the LQG/LTR controller is validated against the reduced-order CDM and high-fidelity SMIB system plant models under various operating conditions, including a three-phase short-circuit fault at the generator terminal and variations in system load. A thorough comparative analysis of the proposed LQG/LTR controller and three nonlinear controllers, EFLC, IEFLC, and PFLC, is conducted regarding stability, transient response, steady-state error, and robustness across different practical operating scenarios.

The simulation findings demonstrate that the proposed LQG/LTR controller provides superior transient response, faster convergence rates, and better control of rotor angle and speed than the EFLC, IEFLC, and PFLC control approaches. Additionally, the LQG/LTR technique enhances robustness by shaping the controller's frequency response, ensuring improved transient stability with guaranteed stability margins under process and measurement noises, severe faults, model mismatches, disturbances, and system overload while remaining simple and computationally efficient. The gain scheduling approach can expand the LQG/LTR controller's operating range and robustness by automatically adjusting the controller gains under different SMIB system operating scenarios. Future work will apply the LQG/LTR controller, enhanced by the gain scheduling mechanism, to multi-machine power systems, such as the IEEE benchmark 10-machine 39-bus New England test system, under severe faults, including a three-phase short-circuit fault at the generator terminal and the tripping of one of the multi-machine power system's transmission lines.

References

[1] C. Canizares et al., "Benchmark models for the analysis and control of small-signal oscillatory dynamics in power systems," *IEEE Transactions on Power Systems*, vol. 32, no. 1, pp. 715-722, Jan. 2017.

[2] G. Gurrala and I. Sen, "Power system stabilizers design for interconnected power systems," *IEEE Transactions on Power Systems*, vol. 25, no. 2, pp. 1042-1051, May 2010.

[3] Z. Deng and C. Xu, "Frequency regulation of power systems with a wind farm by sliding-mode-based design," *IEEE/CAA Journal of Automatica Sinica*, vol. 9, no. 11, pp. 1980-1989, Nov. 2022.

[4] K. Liao and Y. Xu, "A robust load frequency control scheme for power systems based on second-order sliding mode and extended disturbance observer," *IEEE Transactions on Industrial Informatics*, vol. 14, no. 7, pp. 3076-3086, Jul. 2018.

[5] Y. Mi, Y. Fu, C. Wang, and P. Wang, "Decentralized sliding mode load frequency control for multi-area power systems," *IEEE Transactions on Power Systems*, vol. 28, no. 4, pp. 4301-4309, Nov. 2013.

[6] Y. Sun, Y. Wang, Z. Wei, G. Sun, and X. Wu, "Robust H_∞ load frequency control of multi-area power system with time delay: a sliding mode control approach," *IEEE/CAA Journal of Automatica Sinica*, vol. 5, no. 2, pp. 610-617, Mar. 2018.

[7] Y. Wang, D. J. Hill, R. H. Middleton, and L. Gao, "Transient stability enhancement and voltage regulation of power systems," *IEEE Transactions on Power Systems*, vol. 8, no. 2, pp. 620-627, May 1993.

[8] Y. Guo, D. J. Hill, and Y. Wang, "Nonlinear decentralized control of large-scale power systems," *Automatica*, vol. 36, no. 9, pp. 1275–1289, Sep. 2000.

[9] G. Guo, D. J. Hill, and Y.Wang, "Global transient stability and voltage regulation for power systems," *IEEE Transactions on Power Systems*, vol. 16, no. 4, pp. 678–688, Nov. 2001.

[10] L. Gao, L. Chen, Y. Fan, and H. Ma, "A nonlinear control design for power systems," *Automatica*, vol. 28, no. 5, pp. 975–979, Sep. 1992.

[11] Y. Zou, Y. Wang, J. Chen, W. Hu, Y. Zheng, W. Sun, and Z. Xiao, "Optimal Nonlinear Robust Sliding Mode Control of an Excitation System Based on Mixed $\mathcal{H}_2/\mathcal{H}_\infty$ Linear Matrix Inequalities," *Protection and Control of Modern Power Systems*, vol. 9, no. 4, pp. 1–22, Jul. 2024.

[12] M. A. Mahmud, H. R. Pota, M. Aldeen, and M. J. Hossain, "Partial feedback linearizing excitation controller for multimachine power systems to improve transient stability," *IEEE Transactions on Power Systems*, vol. 29, no. 2, pp. 561-571, Mar. 2014.

[13] M.A. Mahmud, "An alternative LQR-based excitation controller design for power systems to enhance small-signal stability," *International Journal of Electrical Power and Energy Systems*, vol. 63, pp. 1–7, Dec. 2014.

[14] M. A. Mahmud, M. J. Hossain, H. R. Pota, and A. M. T. Oo, "Robust partial feedback linearizing excitation controller design for multimachine power systems," *IEEE Transactions on Power Systems*, vol. 32, no. 1, pp. 3-16, Jan. 2017.

[15] T. K. Roy, M. A. Mahmud, W. X. Shen, and A. M. T. Oo, "An adaptive partial feedback linearizing control scheme: An application to a single machine infinite bus system," *IEEE Transactions on Circuits and Systems II: Express Briefs*, vol. 67, no. 11, pp. 2557-2561, Nov. 2020.

[16] T. Mishra, D. Kalke, G. Gurrala, and R. Padhi, "Synchronous Generator Emulation Using Output Matching Control Through Feedback Linearization," *IEEE Transactions on Energy Conversion*, doi: 10.1109/TEC.2025.3536167, Jan. 2025.

[17] Y. Wan and B. Jiang, "Practical nonlinear excitation control for a single-machine infinite-bus power system based on a detailed model," *Automatica*, vol. 62, pp. 18-25, Dec. 2015.

[18] O. Akhrif, F.-A. Okou, L.-A. Dessaint, and R. Champagne, "Application of a multivariable feedback linearization scheme for rotor angle stability and voltage regulation of power systems," *IEEE Transactions on Power Systems*, vol. 14, no. 2, pp. 620-628, May 1999.

[19] J. W. Chapman, M. D. Ilic, C. A. King, L. Eng, and H. Kaufman, "Stabilizing a multimachine power system via decentralized feedback linearizing excitation control," *IEEE Transactions on Power Systems*, vol. 8, no. 3, pp. 830–839, Jun. 2024.

[20] Q. Lu, Y. Sun, Z. Xu, and T. Mochizuki, "Decentralized nonlinear optimal excitation control," *IEEE Transactions on Power Systems*, vol. 11, no. 4, pp. 1957–1962, Nov. 1996.

[21] M. A. Mahmud, H. R. Pota, and M. J. Hossain, "Full-order nonlinear observer-based excitation controller design for interconnected power systems via exact linearization approach," *International Journal of Electrical Power and Energy Systems*, vol. 41, no. 1, pp. 54-62, Oct. 2012.

[22] P. Vernekar, "Nonlinear feedback linearization and LQG/LTR control: a comparative study for a single-machine infinite-bus system," https://doi.org/10.48550/arXiv.2502.10889, Feb. 2025.

[23] T. K. Roy, M. A. Mahmud, and A. M. T. Oo, "Robust adaptive backstepping excitation controller design for higher-order models of synchronous generators in multimachine power systems," *IEEE Transactions on Power Systems*, vol. 34, no. 1, pp. 40-51, Jan. 2019.

[24] Y. Wan and J. Zhao, "Extended backstepping method for single-machine infinite-bus power systems with SMES," *IEEE Transactions on Control Systems Technology*, vol. 21, no. 3, pp. 915-923, May 2013.

[25] S. Huang et al., "Fixed-time backstepping fractional-order sliding mode excitation control for performance improvement of power system," *IEEE Transactions on Circuits and Systems I: Regular Papers*, vol. 69, no. 2, pp. 956-969, Feb. 2022.

[26] J. Zhao, C. Yang, W. Gao, L. Zhou, and X. Liu, "Adaptive optimal output regulation of interconnected singularly perturbed systems with application to power systems," *IEEE/CAA Journal of Automatica Sinica*, vol. 11, no. 3, pp. 595-607, Mar. 2024.

[27] A. C. Zolotas, B. Chaudhuri, I. M. Jaimoukha and P. Korba, "A study on LQG/LTR control for damping inter-area oscillations in power systems," *IEEE Transactions on Control Systems Technology*, vol. 15, no. 1, pp. 151-160, Jan. 2007.

[28] K. M. Son and J. K. Park, "On the robust LQG control of TCSC for damping power system oscillations," *IEEE Transactions on Power Systems*, vol. 15, no. 4, pp. 1306-1312, Nov. 2000.

[29] J. Doyle and G. Stein, "Robustness with observers," *IEEE Transactions on Automatic Control*, vol. 24, no. 4, pp. 607-611, Aug. 1979.

[30] P. Vernekar, Z. Wang, A. Serrani, and K. Passino, "Feedback control methods for a single machine infinite bus system," https://doi.org/10.48550/arXiv.2009.05689, Sep. 2020.

[31] P. M. Anderson and A. A. Fouad, *Power System Control and Stability*. (Second Edition), Hoboken, NJ, USA: Wiley, 2003.